



**HAL**  
open science

## **VEGF counteracts amyloid- $\beta$ -induced synaptic dysfunction**

Pauline Bouvet, Naura Chounlamountri, Chantal Watrin, Roger Besançon, David Meyronet, Jérôme Honnorat, Alain Buisson, Paul Salin, Claire Meissirel

► **To cite this version:**

Pauline Bouvet, Naura Chounlamountri, Chantal Watrin, Roger Besançon, David Meyronet, et al.. VEGF counteracts amyloid- $\beta$ -induced synaptic dysfunction. *Cell Reports*, 2021, 35 (6), pp.109121. 10.1016/j.celrep.2021.109121 . hal-03447499

**HAL Id: hal-03447499**

**<https://hal.science/hal-03447499v1>**

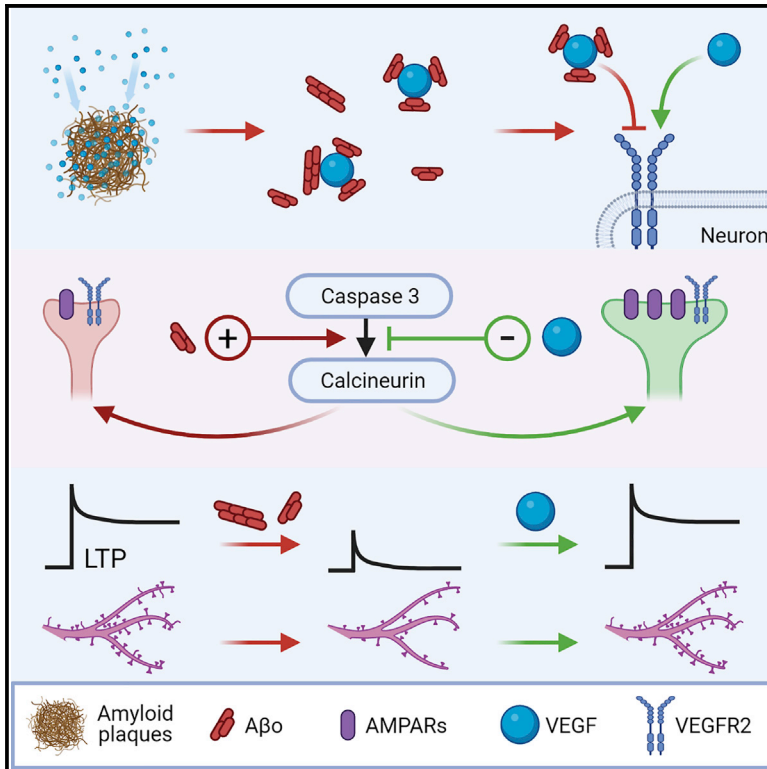
Submitted on 29 Nov 2021

**HAL** is a multi-disciplinary open access archive for the deposit and dissemination of scientific research documents, whether they are published or not. The documents may come from teaching and research institutions in France or abroad, or from public or private research centers.

L'archive ouverte pluridisciplinaire **HAL**, est destinée au dépôt et à la diffusion de documents scientifiques de niveau recherche, publiés ou non, émanant des établissements d'enseignement et de recherche français ou étrangers, des laboratoires publics ou privés.

## VEGF counteracts amyloid- $\beta$ -induced synaptic dysfunction

### Graphical abstract



### Authors

Laurent Martin, Pauline Bouvet, Naura Chounlamountri, ..., Alain Buisson, Paul-Antoine Salin, Claire Meissirel

### Correspondence

claire.meissirel@inserm.fr

### In brief

Martin et al. show that VEGF rescues synaptic dysfunction triggered by A $\beta$  through direct action on synapses. It precludes deleterious activation of the signaling pathways induced by A $\beta$  and restores glutamate-receptor content at synapses. Thus, VEGF preserves hippocampal synaptic plasticity and dendritic spine integrity, which are compromised by A $\beta$ .

### Highlights

- A $\beta$  directly interact with VEGF and impairs VEGFR2 activation
- VEGF prevents A $\beta$ -induced AMPA-R loss and caspase-3-calcineurin activation at synapses
- Hippocampal LTP and LTD impairments due to A $\beta$  are rescued by VEGF
- VEGF counteracts A $\beta$ -induced morphological alteration and loss of dendritic spines



## Article

# VEGF counteracts amyloid- $\beta$ -induced synaptic dysfunction

Laurent Martin,<sup>1,2,7</sup> Pauline Bouvet,<sup>1,2,7</sup> Naura Chounlamountri,<sup>1,2</sup> Chantal Watrin,<sup>1,2</sup> Roger Besançon,<sup>1,2</sup> Delphine Pinatel,<sup>1,2</sup> David Meyronet,<sup>2,3,4</sup> Jérôme Honnorat,<sup>1,2</sup> Alain Buisson,<sup>5</sup> Paul-Antoine Salin,<sup>2,6</sup> and Claire Meissirel<sup>1,2,8,\*</sup>

<sup>1</sup>Institut NeuroMyoGène (INMG), Synaptopathies and Autoantibodies, Institut National de la Santé et de la Recherche Médicale (INSERM), U1217, Centre National de la Recherche Scientifique (CNRS) UMR5310, 69000 Lyon, France

<sup>2</sup>Université Claude Bernard Lyon 1, 69000 Lyon, France

<sup>3</sup>Cancer Research Center of Lyon, Cancer Cell Plasticity, INSERM U1052, CNRS UMR5286, 69000 Lyon, France

<sup>4</sup>Centre de Pathologie et de Neuropathologie Est, Hospices Civils de Lyon 69000 Lyon, France

<sup>5</sup>GIN, INSERM U1216, Université Grenoble Alpes, 38000 Grenoble, France

<sup>6</sup>Lyon Neuroscience Research Center, Forgetting processes and cortical dynamics, INSERM U1028, CNRS UMR5292, 69675 Bron, France

<sup>7</sup>These authors contributed equally

<sup>8</sup>Lead contact

\*Correspondence: [claire.meissirel@inserm.fr](mailto:claire.meissirel@inserm.fr)  
<https://doi.org/10.1016/j.celrep.2021.109121>

## SUMMARY

The vascular endothelial growth factor (VEGF) pathway regulates key processes in synapse function, which are disrupted in early stages of Alzheimer's disease (AD) by toxic-soluble amyloid-beta oligomers (A $\beta$ ). Here, we show that VEGF accumulates in and around A $\beta$  plaques in postmortem brains of patients with AD and in *APP/PS1* mice, an AD mouse model. We uncover specific binding domains involved in direct interaction between A $\beta$  and VEGF and reveal that this interaction jeopardizes VEGFR2 activation in neurons. Notably, we demonstrate that VEGF gain of function rescues basal synaptic transmission, long-term potentiation (LTP), and dendritic spine alterations, and blocks long-term depression (LTD) facilitation triggered by A $\beta$ . We further decipher underlying mechanisms and find that VEGF inhibits the caspase-3-calcineurin pathway responsible for postsynaptic glutamate receptor loss due to A $\beta$ . These findings provide evidence for alterations of the VEGF pathway in AD models and suggest that restoring VEGF action on neurons may rescue synaptic dysfunction in AD.

## INTRODUCTION

Alzheimer disease (AD) is the most common form of dementia among elderly people, and its prevalence increases dramatically with age (Winblad et al., 2016). AD causes a progressive decline in cognitive functions, and memory is one of the earliest functions affected (Dubois et al., 2014). The pathological hallmarks of the disease are extracellular insoluble deposits of amyloid-beta (A $\beta$ ), which form amyloid plaques, together with intracellular neurofibrillary tangles of hyperphosphorylated tau protein in the neurons (Braak and Braak, 1991; Serrano-Pozo et al., 2011). In the early stages of AD, the best neural correlate of cognitive impairments is the hyperactivation and shrinkage of the hippocampal region, associated with the thinning of the posterior cortical regions (Nestor et al., 2004; Putcha et al., 2011). Importantly, brain levels of soluble A $\beta$  were shown to correlate much better than insoluble plaques with the severity of cognitive symptoms in AD, linked with synapse loss (Lue et al., 1999; McLean et al., 1999). Along those lines, compelling evidence has demonstrated that soluble oligomers of A $\beta$  (A $\beta$ o) derived from patients with AD, from mouse or cellular models of the disease, or from synthetic

preparations, have greater toxicity on neurons and synapses than insoluble A $\beta$  forms (Lambert et al., 1998; Walsh et al., 2002; Lesné et al., 2006). A $\beta$ Os are now considered to be the main trigger of the disease (Haass and Selkoe, 2007; Viola and Klein 2015).

Mounting evidence has demonstrated that A $\beta$ o bind to a subset of neurons and, more specifically, target excitatory synapses on dendritic spines (Lacor et al., 2004, 2007). Furthermore, the tracking of membrane-bound A $\beta$ o in living neurons has revealed their ability to diffuse laterally, which results in their concentration in immobile clusters prominently at synapses (Renner et al., 2010). Recently, the combination of high-resolution three-dimensional (3D) imaging and biochemical fractionation approaches demonstrated the accumulation of A $\beta$ o at postsynaptic sites in postmortem human AD brains (Koffie et al., 2012). Furthermore, the use of array tomography has established that A $\beta$ o are not only present in dendritic spines but also inside presynaptic terminals (Pickett et al., 2016). This selective synaptic targeting of A $\beta$ o has generated growing interest in identifying cell-surface proteins, as candidate A $\beta$ o receptors, which can mediate their toxic effect on synapses (Smith and Strittmatter,



2017; Jarosz-Griffiths et al., 2016). The synaptic effect of A $\beta$  has been extensively studied in the hippocampus, *in vivo* and *in vitro*, using synthetic preparations or oligomeric preparations derived from human A $\beta$ -overexpressing cells or from postmortem human AD brains. It consistently causes an impairment in glutamatergic transmission through presynaptic and postsynaptic mechanisms (Ting et al., 2007), including a decrease in release probability at synaptic terminals (He et al., 2019) and dysfunction of postsynaptic glutamate receptors. Importantly, A $\beta$  induce a robust inhibition of long-term potentiation (LTP) (Lambert et al., 1998; Walsh et al., 2002; Shankar et al., 2008) and facilitate long-term depression (LTD). Synaptic strength during LTP largely depends on AMPA receptor (AMPA) trafficking and recruitment to synaptic sites (Ehlers, 2000; Esteban et al., 2003). High brain level of A $\beta$  in transgenic models of the disease was shown to trigger the internalization and synaptic removal of AMPAR, leading to synaptic depression (Almeida et al., 2005; Hsieh et al., 2006; Alfonso et al., 2014). Underlying mechanisms have been investigated and involve the upregulation of AMPAR ubiquitination and their dephosphorylation at serine 845 residue (S845) on the carboxy terminal of GluA1 subunit (Hsieh et al., 2006; Rodrigues et al., 2016). Furthermore, the phosphorylation state of GluA1 on S845 was shown to be critical for LTD and potentially involved in LTP (Lee et al., 2010a). Thus, A $\beta$ -induced changes in these molecular processes are thought to result in synaptic plasticity impairments and in cognition deficits associated with AD.

The canonical angiogenic factor VEGF was shown to regulate several neurobiological processes in the adult brain, with a key role in promoting hippocampal synaptic plasticity and memory consolidation in mice (Cao et al., 2004; Kim et al., 2008; Licht et al., 2011; De Rossi et al., 2016). VEGF overexpression obtained by intracerebral administration, gene transfer, or in conditional transgenic mice improves associative memory performances (Cao et al., 2004; Licht et al., 2011), and short exposure to overexpressed VEGF is sufficient to affect cognitive function, independent of its effect on neurogenesis and angiogenesis (Licht et al., 2011). Recent studies with genetically engineered mouse models have further demonstrated that the VEGF receptor VEGFR2 is expressed in hippocampal neurons *in vivo* (De Rossi et al., 2016; Harde et al., 2019; Luck et al., 2019) and is required for hippocampal-dependent forms of LTP and consolidation of memory (De Rossi et al., 2016). In addition, we have reported that sustained activity in the hippocampus is able to trigger a rapid increase in endogenous VEGF release, which strongly suggests that activity-dependent secretion of VEGF is involved in synaptic plasticity (De Rossi et al., 2016). Thus, the VEGF-VEGFR2 pathway, aside from its well-known effect on brain blood vessels, has a powerful and direct impact on synapse structure and function.

Importantly, higher levels of VEGF in cerebrospinal fluid (CSF) have been associated, during human aging, with increased hippocampal volume and improved cognitive performances over time (Hohman et al., 2015). Furthermore, in the presence of enhanced AD biomarkers in CSF, elevated VEGF levels are associated with less cognitive decline (Hohman et al., 2015), highlighting a potential neuroprotective role for VEGF in AD. Indeed, in transgenic mouse models of the disease, VEGF triggers func-

tional rescue in hippocampus-dependent learning and memory through a decrease in A $\beta$ -mediated endothelial-cell alterations and changes in brain vascularization (Garcia et al., 2014; Religa et al., 2013; Herrán et al., 2013). However, it remains to be demonstrated whether VEGF can exert a direct protective action on synapses challenged by A $\beta$  through its receptors expressed on neurons.

Based on the current knowledge of VEGF involvement in synapse strengthening and memory consolidation, we proposed that VEGF is ideally poised to rescue synaptic alterations and related cognitive deficits initiated by toxic A $\beta$ . We hypothesized that increasing VEGF levels in the hippocampus would attenuate synaptic dysfunction triggered by A $\beta$  through direct action of VEGF on synapses. We therefore analyzed VEGF expression patterns in postmortem human AD brains and in a transgenic mouse model of the disease to determine to what extent the VEGF pathway is affected in the disease. In addition, we developed a mechanistic approach by combining electrophysiological, 3D cell imaging, subcellular fractionation, and protein-protein interaction techniques to investigate the effect of VEGF on the synaptic signature of A $\beta$ -mediated toxicity in AD.

## RESULTS

### Accumulation of VEGF in amyloid plaques

Abnormal levels of VEGF have been associated with A $\beta$  deposition in Alzheimer's disease (Thomas et al., 2015), and our goal was to decipher the spatial relationship between endogenous VEGF and insoluble A $\beta$  plaques in the postmortem frontal cortex from AD cases and control patients (Table S1). As expected, amyloid plaques containing insoluble A $\beta$  were identified only in the cortex of AD patients, and high VEGF immunoreactivity was detected in the blood vessels from both AD and control patients (Figure 1A). Double-labeled immunostaining showed that VEGF and A $\beta$  were expressed in partially overlapping patterns centered on insoluble A $\beta$ <sup>+</sup> plaques, with reduced VEGF expression at a distance from the plaques. To study the relationship between VEGF and A $\beta$  in the microenvironment of A $\beta$  plaques, we used antibodies recognizing VEGF and fibrillar A $\beta$ , respectively (Figure 1B). VEGF was found to be associated with OC<sup>+</sup> A $\beta$  species, which display a conformation-dependent epitope (Kayed et al., 2007; Chiang et al., 2018) in the immediate vicinity of human brain deposits (Figure 1B). This finding is consistent with a co-localization between VEGF and fibrillar A $\beta$ . In addition, high VEGF immunoreactivity was detected in ramified cells located in the peri-plaque area (Figure 1A). To identify reactive astrocytes and activated microglial cells, we immunolabeled AD brain sections for VEGF and GFAP or CD68 (Figures 1C–1E). We observed GFAP<sup>+</sup> astrocytes and CD68<sup>+</sup> microglia in the peri-plaque area of Thioflavin-S-stained dense-core plaques, with some GFAP<sup>+</sup> astrocytes expressing VEGF (Figures 1C and 1E).

We further assessed whether co-localization of VEGF and A $\beta$  could be replicated in the *APP/PS1-21* mouse model of AD during the early stages of A $\beta$  deposition. Plaque load was characterized by Thioflavin S staining in brain sections from 4-month-old *APP/PS1* mice. Assessment of amyloid burden (Figure S1A) confirmed previous findings (Radde et al., 2006),

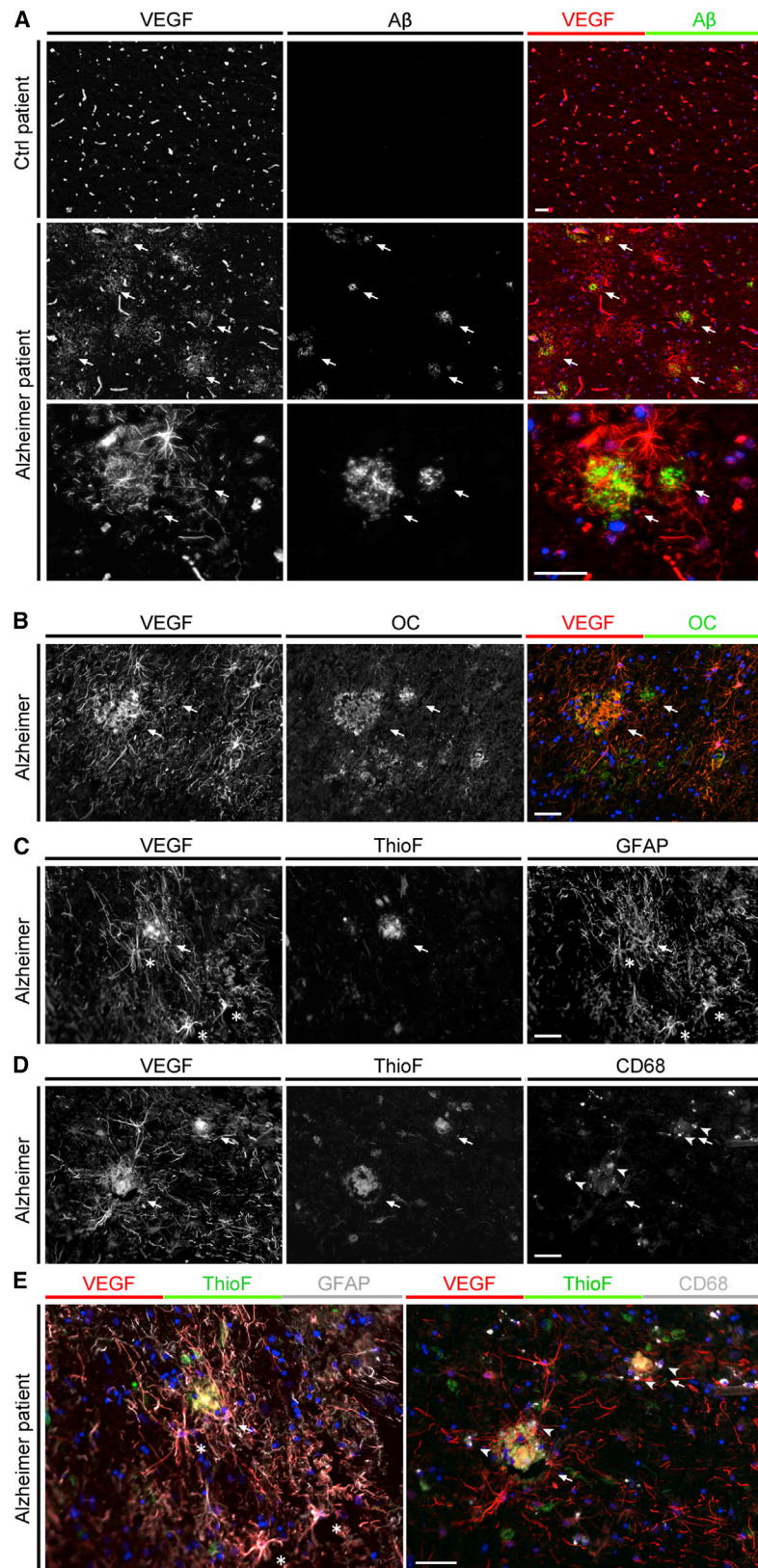


**Figure 1. Association of VEGF expression with A $\beta$  plaques**

(A) Immunostainings in postmortem brain sections from AD and control patients showing VEGF expression (red) in relation to A $\beta$  deposits (green). Note the VEGF staining centered on the A $\beta$  plaques indicated by arrows, with VEGF<sup>+</sup> cells in their vicinity (merge).

(B) Representative images showing A $\beta$  deposits double labeled for VEGF (red) and fibrillar A $\beta$  (OC, green, arrows).

(C) Example of a dense-core A $\beta$  plaque labeled with Thioflavin-S (ThioF, arrow) with reactive astrocytes positive for both VEGF and GFAP in the peri-plaque area (asterisks).

(D) Relationship between Thioflavin-S<sup>+</sup> plaques (ThioF, arrows), activated microglial cells positive for CD68 (arrowheads), and VEGF immunostaining showing activated microglial cells concentrated around dense-core plaques but negative for VEGF.

(E) Left, merged image of the three stains shown in (C) with VEGF (red), Thioflavin-S (green), and GFAP (gray), showing reactive astrocytes expressing VEGF. Right, merged image of the three stains illustrated in (D) showing no colocalization between VEGF and CD68, indicating that reactive microglial cells do not express VEGF.

Scale bars, 50  $\mu$ m.

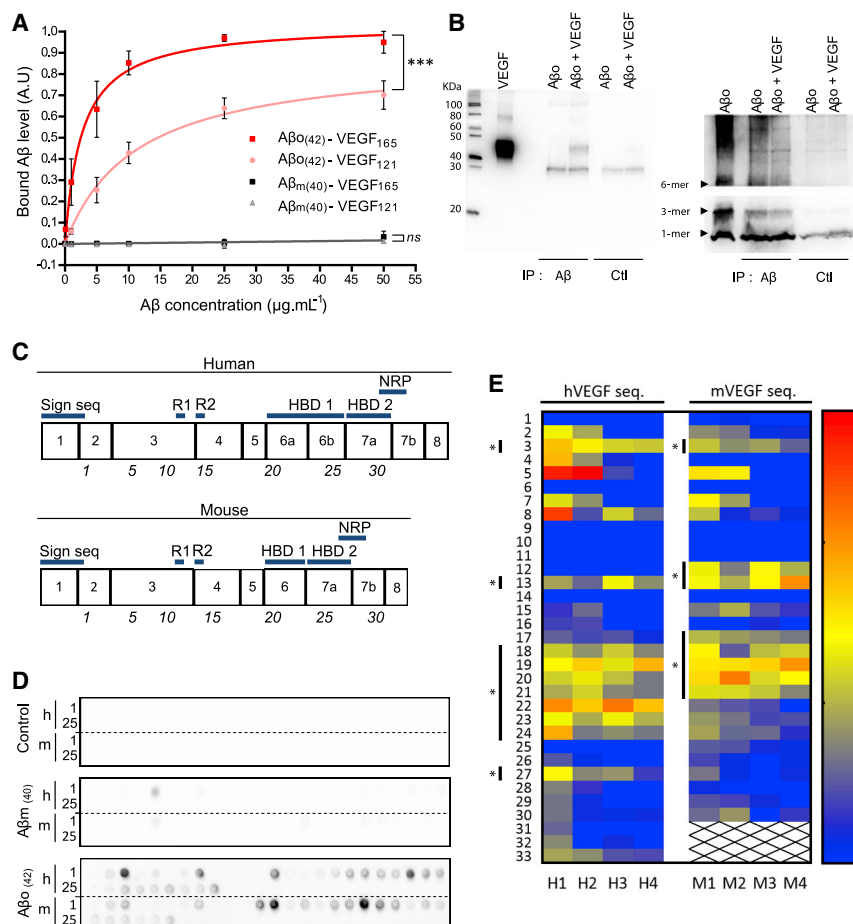


**Figure 2. Selective binding of Aβ oligomers to VEGF and identification of the binding sites, with ELISA and peptide arrays used to analyze Aβ binding to VEGF**

(A) Dose-dependent binding of biotinylated forms of Aβ<sub>42</sub> oligomers (Aβ<sub>o</sub>) or Aβ<sub>40</sub> monomers (Aβ<sub>m</sub>) to VEGF<sub>165</sub> and VEGF<sub>121</sub> isoforms, analyzed by ELISA. Each value represents the means ± SEM between three independent experiments. \*\*\*p < 0.001.

(B) Aβ<sub>o</sub> ± biotinylated VEGF<sub>165</sub> was immunoprecipitated with an anti-Aβ or control antibody followed by immunoblotting for VEGF (left) or Aβ (right, short exposure [bottom]); representative immunoblots showing that VEGF coimmunoprecipitates with Aβ<sub>o</sub>. VEGF<sub>165</sub> and Aβ<sub>o</sub> are used as positive controls, and Aβ monomers (1-mer), trimers (3-mer), and hexamers (6-mer) are indicated by arrowheads.

(C) Human and murine DNA exon sequences coding for VEGF, with Sign seq: signal sequence; R1 and R2: VEGFR1 and VEGFR2 binding sites; HBD 1 and 2: heparin binding domains 1 and 2; NRP: neuropilin binding site. Italic numbers refer to the position of the peptide spotted on the peptide array.

(D) Representative peptide arrays showing Aβ interacting sites in the VEGF protein sequence with biotinylated Aβ<sub>o</sub> or Aβ<sub>m</sub>, and vehicle (control). n = 4 independent experiments.

(E) Heatmap illustrating the three main binding domains between Aβ<sub>o</sub> and VEGF (asterisks) with values normalized to the maximum binding and illustrated by a blue-to-red color code from low to high levels of binding. h: human; m: murine. H1 to H4 and M1 to M4 represent the four experiments.

with 0.53% ± 0.28% (n = 3, means ± SEM) of the neocortical area occupied by fibrillar Aβ plaques (Ulrich et al., 2014). Furthermore, analysis of VEGF immunostaining revealed that 20.79% ± 5.28% of these amyloid plaques were positive for VEGF (n = 3; Figure S1B), a proportion which increased to 39.39% ± 2.90% in 8-month-old APP/PS1 mice (n = 3; Figure S1C). These results suggested that Aβ-VEGF interaction is present in insoluble Aβ deposits from the early stages of Aβ deposition and that this trapping increases with Aβ burden.

### Aβ oligomers directly interact with matrix-binding and diffusible VEGF isoforms

To determine to what extent VEGF also associates with the soluble pool of Aβ, we prepared synthetic Aβ<sub>42</sub> oligomers (Aβ<sub>o</sub>) and Aβ<sub>40</sub> monomers (Aβ<sub>m</sub>) and investigated their binding abilities to soluble VEGF isoforms, VEGF<sub>121</sub> and VEGF<sub>165</sub>. We first validated Aβ<sub>o</sub> preparations using standard biochemical analyses and characterized their structure with transmission electron microscopy (Figures S2A and S2B). Next, an ELISA assay revealed that Aβ<sub>m</sub> failed to bind to immobilized VEGF<sub>121</sub> or VEGF<sub>165</sub>. In contrast, Aβ<sub>o</sub> were able to bind to both isoforms, demonstrating direct interactions with VEGF<sub>121</sub> or VEGF<sub>165</sub>. However, Aβ<sub>o</sub> binding was significantly less with VEGF<sub>121</sub> (Figure 2A), indicating that VEGF<sub>165</sub> has additional binding sites for Aβ<sub>o</sub>. Aβ<sub>o</sub> interaction

with VEGF<sub>165</sub> was further confirmed with co-immunoprecipitation experiments (Figure 2B). Finally, the binding ability of the long VEGF<sub>189</sub> isoform, which displays an additional heparin-binding domain compared with VEGF<sub>165</sub> (Ferrara et al., 2003) was assessed. Our findings indicated that heparin-binding isoforms display the most potent binding to Aβ<sub>o</sub>, with VEGF<sub>165</sub> showing an intermediate binding ability between the less-diffusible VEGF<sub>189</sub> and the freely diffusible, non-heparin-binding VEGF<sub>121</sub> (compare Figures 2A and S2C)

To further characterize which domains of the VEGF isoforms bind to Aβ<sub>o</sub>, we designed peptide arrays that encompassed the entire protein sequence of human and murine VEGF (Figure 2C). Peptide arrays were incubated with biotinylated Aβ<sub>m</sub>, Aβ<sub>o</sub>, or vehicle, and positive binding sites were visualized as dark, labeled spots. Our data showed that Aβ<sub>o</sub> induced strong labeling of specific spots distributed over the human and murine protein sequences (Figure 2D). In contrast, almost no labeling was obtained with Aβ<sub>m</sub>, except for one weak spot. A heatmap revealed that there were three main sites of human and murine VEGF-bound Aβ<sub>o</sub>, namely the N-terminal part, the VEGFR2-binding site, and heparin binding domain 1 (HBD 1) with a slight involvement of HBD 2 (Figure 2E). These data are consistent with our ELISA findings showing that VEGF<sub>189</sub> expressing HBD 1 and HBD 2 has additional binding sites for Aβ<sub>o</sub> compared with

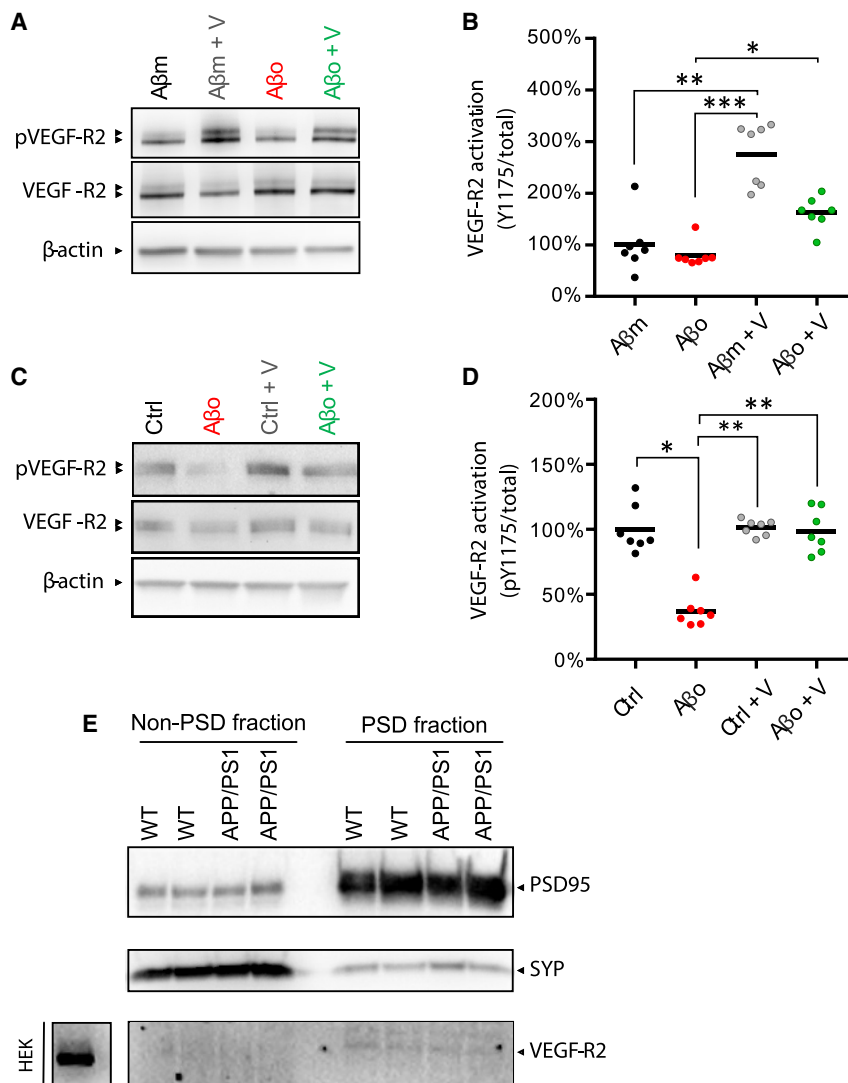


**Figure 3. A $\beta$  oligomers disrupt VEGFR2 activation, with receptor activation assessed by western blotting and expressed as the ratio between phosphorylated VEGFR2 (Y<sub>1175</sub>) and total receptor expression**

(A) Representative immunoblotting for pVEGFR2, total VEGFR2, and actin in VEGFR2-expressing HEK cells treated with A $\beta$ <sub>42</sub> monomers (A $\beta$ m) or A $\beta$ <sub>42</sub> oligomers (A $\beta$ o) at 1  $\mu$ M for 5 min, in presence or absence of 50 ng  $\cdot$  mL<sup>-1</sup> VEGF. (B) VEGF-induced VEGFR2 activation when associated with A $\beta$ m (Kruskal-Wallis,  $p = 0.00013$ ; post hoc  $p < 0.01$ ,  $n = 7-7$ ) and with A $\beta$ o (post hoc  $p < 0.05$ ,  $n = 7-7$ ), but A $\beta$ o tended to reduce that activation. (C) Representative immunoblotting for pVEGFR2, total VEGFR2, and actin in hippocampal neurons treated with a control peptide (Ctrl) or A $\beta$ o at 1  $\mu$ M for 1 h  $\pm$  50 ng  $\cdot$  mL<sup>-1</sup> VEGF. (D) A $\beta$ o reduced VEGFR2 activation in neurons (Kruskal-Wallis,  $p = 0.0013$ ; post hoc  $p < 0.05$ ,  $n = 7-7$ ) but VEGF rescued it (post hoc  $p < 0.01$ ,  $n = 7-7$ ). \* $p < 0.05$ , \*\* $p < 0.01$ , \*\*\* $p < 0.001$ . (E) Representative western blot of hippocampal PSD and non-PSD fractions from 8-month-old APP/PS1 and WT mice immunoblotted for synaptophysin, PSD95, and VEGFR2. VEGFR2-expressing HEK cell lysate was used as a positive control.

VEGF<sub>165</sub> expressing only HBD 2 and with VEGF<sub>121</sub>, which lacked both HBD 1 and HBD 2.

### VEGF counteracts A $\beta$ -induced impairment in VEGFR2 activation

To investigate whether A $\beta$  impede VEGFR2 signaling mediated by VEGF, we examined receptor activation in HEK cells engineered to overexpress VEGFR2, and acutely treated with A $\beta$ m or A $\beta$ o,  $\pm$  VEGF. Western blotting analyses showed that basal VEGFR2 activation was not affected by treatments. In contrast, VEGF induced VEGFR2 activation in all conditions, as revealed by the increased phosphorylation of VEGFR2 Y<sub>1175</sub> (Figures 3A and 3B). However, acute A $\beta$ o treatment tended to decrease the VEGF-dependent VEGFR2 activation (Figures 3A and 3B), suggesting that A $\beta$ o may inhibit VEGF binding to VEGFR2. To assess whether the A $\beta$ -VEGF interaction impairs VEGFR2 activation in physiological conditions, we used cultured hippocampal neurons exposed for 1 h to A $\beta$ o or control peptides,  $\pm$

VEGF. ELISA quantification showed that endogenous VEGF is released in the culture medium (638  $\pm$  0.02 pg VEGF per mL;  $n = 6$ ) and can stimulate VEGFR2 expressed on hippocampal neurons (De Rossi et al., 2016). With A $\beta$ o treatment VEGFR2 phosphorylation was significantly reduced compared with the control condition, indicating that receptor activation by endogenous VEGF was impaired (Figures 3C and 3D). To determine whether increasing VEGF levels might reverse that deficit in VEGFR2 activation, we stimulated hippocampal neurons with a combined A $\beta$ o and VEGF treatment. Immunoblotting analyses revealed that the combined treatments normalized VEGFR2 activation to control levels and prevented the A $\beta$ o-induced decrease (Figures 3C and 3D). Taken together, these data demonstrated that A $\beta$ o reduced VEGFR2 phosphorylation only in the presence of its ligand, but exogenous application of VEGF counteracted that reduction in VEGFR2 activation. Thus, these findings suggested that A $\beta$ -VEGF binding interactions might have an important role in regulating VEGFR2 activation in a pathological context.

To further determine the relevance of neuronal VEGFR2 in the APP/PS1 mouse model of AD, we performed brain-tissue fractionation to isolate the synaptic compartment from the hippocampus of APP/PS1 and wild-type (WT) mice. Then, in these two groups, we compared VEGFR2 expression in postsynaptic density (PSD) and non-PSD-enriched fractions derived from

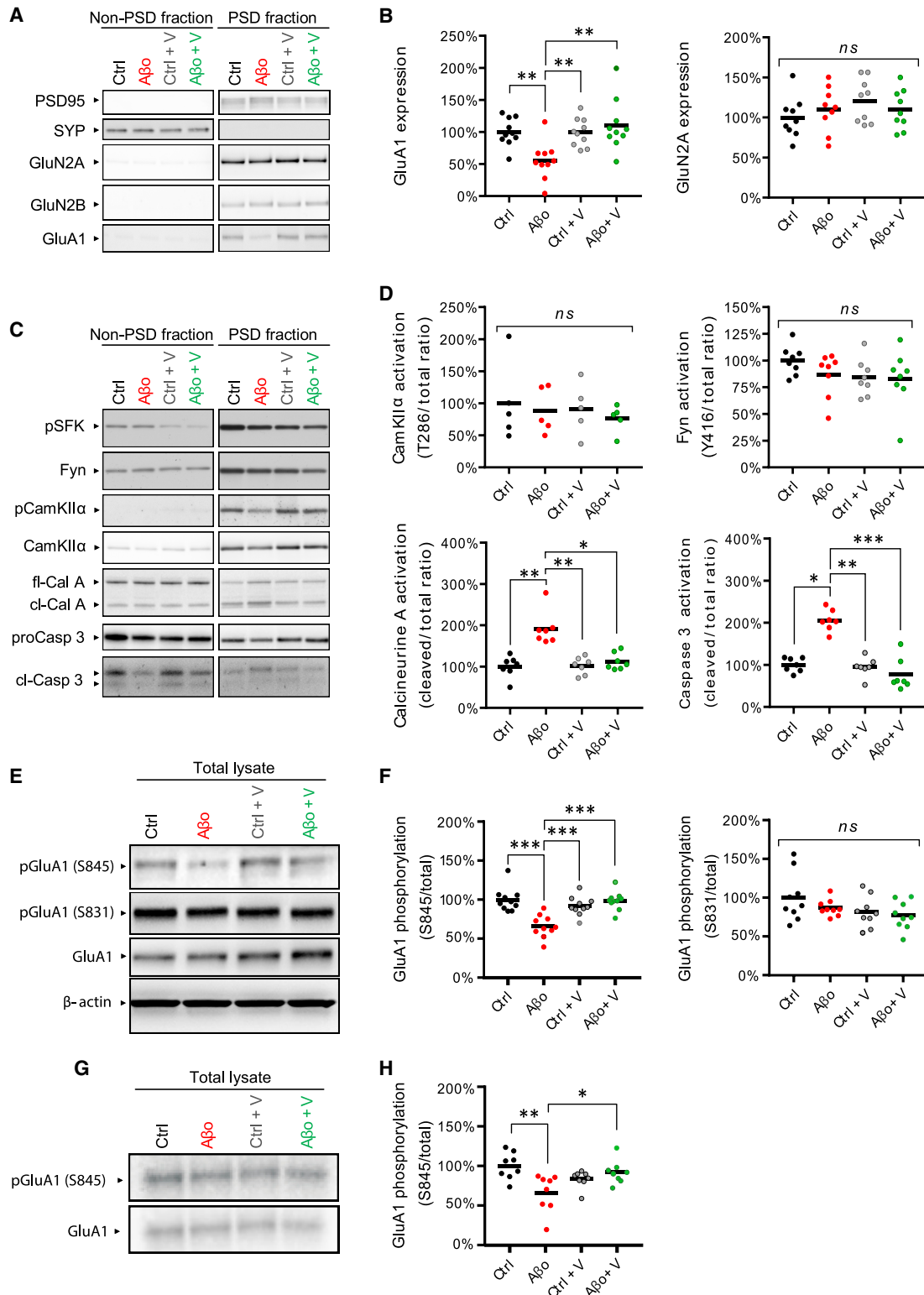


**Figure 4. VEGF counteracts AMPAR loss and phosphatase/protease activation at synapses and rescues AMPAR phosphorylation**

(A–D) PSD and non-PSD fractions were isolated from hippocampal neuronal cultures treated for 1 h with control peptides (Ctrl) or A $\beta$  at  $1 \mu\text{M} \pm 50 \text{ ng} \cdot \text{mL}^{-1}$  VEGF, and analyzed for receptor and signaling protein content. (A) Representative western blot immunoblotted for PSD95, synaptophysin (SYP), GluN2A,

(legend continued on next page)

hippocampal synaptosomes. These fractions were validated by the predominant expression of the postsynaptic density marker PSD95 and the presynaptic marker synaptophysin, respectively (Figure 3E). Our data showed that VEGFR2 expression level was similar in the hippocampus from 8-month-old WT and *APP/PS1* mice and was predominant in PSD fractions (Figure 3E). They validated VEGFR2 expression at the excitatory synaptic level in the hippocampus of *APP/PS1* mice at advanced stages of A $\beta$  deposition. They further demonstrated that the VEGF/VEGFR2 pathway is compromised in hippocampal neurons by high level of toxic, soluble A $\beta$  forms.

Next, we assessed whether VEGF triggers a decrease in A $\beta$  synaptic targeting. We analyzed A $\beta$  cell surface staining on hippocampal neurons treated for 30 min with biotinylated A $\beta$ m (used as a control) or A $\beta$ o,  $\pm$  VEGF. Synapses were identified with the presynaptic marker Bassoon and the postsynaptic marker PSD95, and the biotinylated A $\beta$  was identified with streptavidin. A $\beta$ -cell-surface staining dramatically increased with A $\beta$ o compared with A $\beta$ m treatments (Figure S3A), confirming that A $\beta$ o selectively bound to the hippocampal neuron surface. Furthermore, quantification of colocalized Bassoon and PSD95 synaptic clusters with A $\beta$  staining indicated that exogenous VEGF does not prevent A $\beta$  synaptic targeting (Figure S3B). Thus, VEGF is able to counteract A $\beta$ -dependent inhibition of neuronal VEGFR2 activation without impeding A $\beta$  synaptic targeting.

### VEGF rescues the synaptic content in glutamate receptors challenged by A $\beta$ o

VEGFR2 signaling in neurons is directly implicated in glutamate receptor content at synapses by triggering synaptic incorporation of AMPA and NMDA receptors (De Rossi et al., 2016). In addition, evidence indicates that synaptic glutamate receptors are internalized in response to soluble A $\beta$ o (Hsieh et al., 2006). Thus, we examined whether A $\beta$ o-induced loss of glutamate receptors at synapses can be counteracted by VEGFR2 signaling in response to VEGF. Subcellular fractionation (De Rossi et al., 2016; El Gaamouch et al., 2012) was used to determine glutamate receptor content at synapses in hippocampal cultures treated with A $\beta$ o or control peptides,  $\pm$  VEGF. We validated the PSD purification protocol with the expression of PSD95 and synaptophysin in PSD and non-PSD fractions, respectively (Figure 4A). Immunoblotting showed that the expression levels of GluN2A and GluN2B NMDA receptor subunits were similar in all conditions in PSD fractions (Figures 4A and 4B). In contrast, the content in GluA1 AMPAR subunits was significantly reduced

after A $\beta$ o treatment compared with that of the control (Figures 4A and 4B), in agreement with previous reports (Almeida et al., 2005; Hsieh et al., 2006). Importantly, co-administration of A $\beta$ o and VEGF prevented that decrease in postsynaptic AMPAR (Figures 4A and 4B), demonstrating that VEGF prevents A $\beta$ o-dependent removal of GluA1 from postsynaptic sites.

### VEGF effect involves a downregulation of the caspase-3-calcineurin pathway

To investigate the molecular mechanisms underlying GluA1 redistribution at synapses, we examined the signaling pathways activated by A $\beta$ o and/or VEGF. The activation of the caspase-3-calcineurin pathway has been involved in the regulation of GluA1-receptor internalization at synapses (Hsieh et al., 2006) and, in synaptic impairment in a mouse model of AD, via the selective removal of GluA1 from postsynaptic sites (D'Amelio et al., 2011). Thus, given the key role of this pathway, we analyzed its expression and activation in PSDs purified from treated hippocampal cultures. Caspase-3 and calcineurin A activation was assessed with the expression ratio between their cleaved active form (cl) and their inactive pro-form (pro) or their full-length form (fl), using dedicated antibodies. A $\beta$ o application resulted in a significant increase in caspase-3 and calcineurin activation in PSDs compared with the control condition (Figures 4C and 4D), consistent with the reported increase in caspase-3 activity in synaptosomes derived from transgenic AD mice (D'Amelio et al., 2011). In contrast, combined A $\beta$ o and VEGF treatment counteracted A $\beta$ o-induced activation and normalized both caspase-3 and calcineurin A activation ratios (Figures 4C and 4D). In addition, we monitored CaMKII activation, which promotes GluA1-receptor anchorage at synapses (Opazo et al., 2010), as well as Src family kinase activity for their major roles in NMDA-receptor regulation (Salter and Kalia, 2004). None of the applied treatments had an effect on Fyn or CaMKII activation compared with the control condition (Figures 4C and 4D). Thus, collectively, these findings underscore that VEGF limits the activation of the caspase-3-calcineurin pathway at postsynaptic sites in neurons challenged by A $\beta$ o.

### VEGF restores GluA1 phosphorylation and cell surface expression impeded by A $\beta$ o

Mobilizing new AMPARs to synapses in response to synaptic activity critically depends on their phosphorylation status (Lee et al., 2000a). Moreover, their dephosphorylation triggered by calcineurin results in their removal from postsynaptic sites and internalization (Miñano-Molina et al., 2011). Therefore, we

GluN2B, and GluA1 subunits. (B) GluA1 and GluN2A expression levels normalized to the control, showing GluA1 expression reduced by A $\beta$ o (Kruskal-Wallis,  $p = 0.0022$ ; post hoc  $p < 0.01$ ,  $n = 10-10$ ) but rescued by VEGF (post hoc  $p < 0.01$ ,  $n = 10-10$ ). (C) Representative immunoblotting for activated and total form of Fyn, CaMKII $\alpha$ , calcineurin A (Cal A), and caspase-3 (Casp-3). (D) A $\beta$ o increased caspase-3 and calcineurin A activation (Casp-3: Kruskal-Wallis,  $p = 0.0008$ ; post hoc  $p < 0.05$ ,  $n = 7-7$ ; Cal A, Kruskal-Wallis,  $p = 0.0014$ ; post hoc  $p < 0.01$ ,  $n = 7-7$ ), but VEGF prevented it (Casp-3, post hoc  $p < 0.001$ ,  $n = 7-7$ ; Cal A, post hoc  $p < 0.05$ ,  $n = 7-7$ ).

(E) AMPAR phosphorylation and total expression levels were analyzed in extracts from treated hippocampal neuronal cultures with representative immunoblotting shown for phosphorylated GluA1 (S845 and S831), total GluA1, and actin.

(F) Ratio between phosphorylated GluA1 at S845 or S831 and total GluA1 expression showing a reduction in S845 phosphorylation because of A $\beta$ o (one-way ANOVA,  $p < 0.0001$ ; post hoc  $p < 0.0001$ ,  $n = 10-10$ ) but prevented by VEGF (post hoc  $p < 0.0001$ ,  $n = 10-10$ ).

(G) Representative immunoblot of S845 phosphorylation in 21-DIV hippocampal cultures with complex networks.

(H) S845 phosphorylation was reduced by A $\beta$ o (Kruskal-Wallis,  $p = 0.0069$ ; post hoc  $p < 0.01$ ,  $n = 8-8$ ) but rescued by VEGF (post hoc  $p < 0.05$ ,  $n = 8-8$ ). ns: not significant, \* $p < 0.05$ , \*\* $p < 0.01$ , \*\*\* $p < 0.001$ .

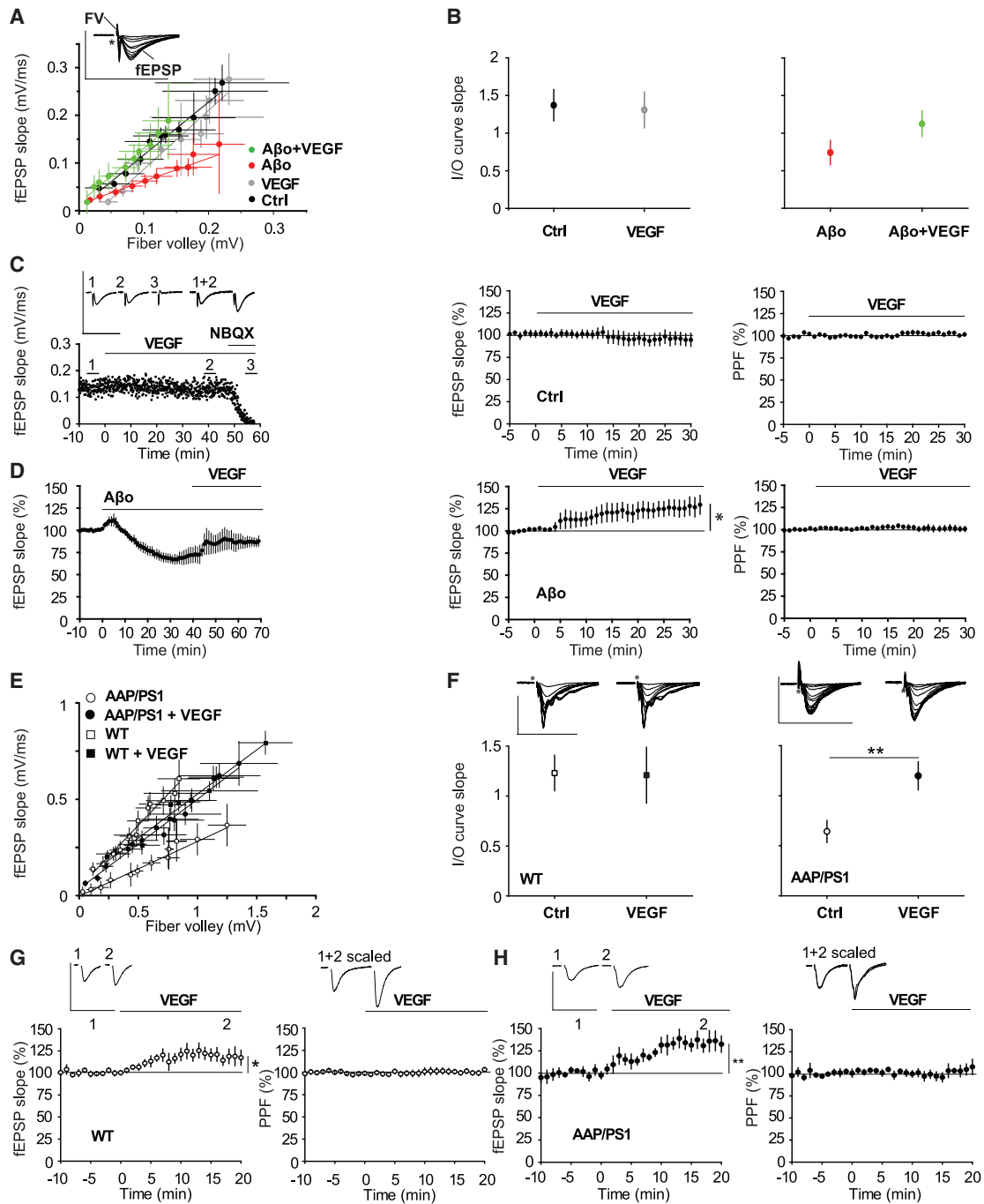


**Figure 5. VEGF increased synaptic transmission in  $\beta$ -amyloid treated slices and in slices from *APP/PS1* mice**

(A) Averaged input-output (I/O) curves obtained in control (black), VEGF (gray),  $A\beta_0$  (red, 500 nM), and  $A\beta_0$ +VEGF (green) groups linking fiber volley amplitude to the synaptic response slope. A linear regression was computed on averaged I/O curves of five experiments in each of the control-, VEGF-,  $A\beta_0$ -, and  $A\beta_0$ +VEGF-treated group. FV: fiber volley; fEPSP: field excitatory postsynaptic potential.

(B) Averaged I/O curve slopes showing no significant modulation by VEGF in control or  $A\beta_0$ -treated slices ( $p > 0.05$ , unpaired t test).

(C) VEGF did not modify fEPSP in control slices (ns, paired t test,  $n = 5$  mice). Left, typical time course before (1) and after (2) VEGF with fEPSP mediated by AMPAR (3) NBQX, 5  $\mu$ M. VEGF did not change paired-pulse facilitation ratio (PPF) in control slices (superimposed 1 and 2).

(D) fEPSPs were decreased by  $A\beta_0$  and partially restored by VEGF (middle,  $p = 0.027$ , paired t test,  $n = 7$ ) with no change in PPF (right).

(E) I/O curve in 8-month-old *APP/PS1* and WT mice showing averaged I/O curve slopes in WT-, WT+VEGF-, *AAP/PS1*-, and *AAP/PS1*+VEGF-treated groups.

(legend continued on next page)

immunoblotted total hippocampal lysates after A $\beta$  or control treatments,  $\pm$  VEGF, to examine GluA1 phosphorylation at major sites known to regulate receptor trafficking: S831 and S845 (Esteban et al., 2003; Roche et al., 1996; Malinow 2003). A $\beta$  treatments caused a significant reduction in the level of phosphorylated GluA1 S845 compared with the control condition (Figures 4E and 4F), as previously reported (Miñano-Molina et al., 2011). However, when VEGF was associated with A $\beta$ , it significantly enhanced levels of S845 phosphorylation compared with that of A $\beta$  alone (Figures 4E and 4F). Importantly, these effects were specific for S845 phosphorylation as the different treatments failed to induce a change in S831 phosphorylation of GluA1 (Figures 4E and 4F). To extend those results, we used hippocampal neurons at 21 days *in vitro* (DIV) with complex networks and applied A $\beta$  at 500 nM for 12 h to trigger a deficit in S845 GluA1 phosphorylation, as previously reported (Jin and Selkoe, 2015). We found that A $\beta$  significantly reduced S845 phosphorylation level by 33.8% compared with the control condition (Figures 4G and 4H), whereas VEGF and A $\beta$  co-application preserved it (Figures 4G and 4H). In addition, adult hippocampal slices treated with A $\beta$  showed a significant reduction in GluA1 phosphorylation after chemical LTP compared with slices treated with VEGF, indicating that A $\beta$  and VEGF exert opposite effects on GluA1 phosphorylation (Figure S4A).

Furthermore, because S845 phosphorylation directly contributes to GluA1 trafficking to the cell surface (Esteban et al., 2003), we selectively labeled the surface pool of GluA1 in hippocampal cultures exposed to A $\beta$  and/or VEGF treatments (Figure S4B). Quantitative imaging showed that A $\beta$  reduced the average size of GluA1 clusters compared with that of the control condition (Figure S4C), recapitulating the loss of surface GluA1 reported by others (Zhao et al., 2010). Conversely, we showed that combined A $\beta$  and VEGF treatment prevented A $\beta$ -induced reduction in cluster size and restored them to control values (Figure S4C). Altogether, our current data indicate that GluA1 trafficking and related phosphorylation processes are controlled in the opposite way, depending on whether A $\beta$  are associated with VEGF or not.

### VEGF rescues A $\beta$ -induced impairment in synaptic transmission and plasticity

The pool of phosphorylated GluA1 S845-containing AMPAR is found at significant levels in PSD fractions of the adult mouse forebrain under basal condition of activity and reaches 14.2% of GluA1-expressing receptors in total membrane fractions (Diering et al., 2016). Given that those GluA1 S845 receptors are preferentially inserted and/or stabilized at the neuronal cell surface and are primed for synaptic targeting (Oh et al., 2006), it raises the question of the effect of A $\beta$  and VEGF on basal synaptic transmission. Thus, we investigated the effect of VEGF on basal synaptic transmission in the adult hippocampus confronted by acute or chronic A $\beta$  toxicity. Synaptic transmission was analyzed at the Schaffer collateral to CA1 synapse in acute hip-

poampal slices from WT mice treated with A $\beta$  and/or VEGF (Figure 5A). VEGF did not modulate the input/output (I/O) curves in control slices (Figure 5B). However, the I/O curve tended to increase in the A $\beta$  + VEGF condition compared with that of A $\beta$  alone, but without reaching statistical significance (Figure 5B). These results led us to examine A $\beta$  effect on synaptic transmission before and after VEGF application. VEGF did not change the basal synaptic transmission in control condition (Figure 5C). In contrast, evoked responses displayed a biphasic pattern upon A $\beta$  administration, with an initial and transient increase in field excitatory postsynaptic potential (fEPSP) slope, followed by a sustained decrease, which was partially but significantly reversed by VEGF (Figure 5D). Furthermore, no change in paired-pulse facilitation (PPF) was observed upon VEGF and A $\beta$  treatment (Figure 5D), suggesting that the VEGF-induced synaptic increase was mediated by postsynaptic mechanisms. Thus, the ability of VEGF to partially restore the deficit in synaptic transmission induced by A $\beta$  over time may involve a postsynaptic mechanism, in agreement with its effect on AMPAR phosphorylation.

To further highlight the *in vivo* relevance of VEGF in basal synaptic transmission rescue, we used 8-month-old WT and *APP/PS1* mouse model of AD, when deficits in synaptic function have first been reported (Gengler et al., 2010). We found that basal synaptic transmission was reduced by 52.3% in the *APP/PS1* transgenic mice (Figures 5E and 5F), and this reduction was counteracted by VEGF application (Figures 5E and 5F). Time-course analyses further revealed that the mean fEPSP slope was significantly increased shortly after VEGF application in *APP/PS1* and in WT slices (Figures 5G and 5H). This VEGF-dependent increase in mean fEPSP slopes was not associated with a change in PPF (Figures 5G and 5H).

Overall, our data demonstrated the importance of VEGF in restoring the strength of basal synaptic transmission when hippocampal synapses are challenged by toxic A $\beta$ , either during acute exposure or chronically in the *APP/PS1* model of AD.

Accumulating evidence indicates that GluA1 trafficking and phosphorylation processes also have a critical role in synaptic plasticity (Citri and Malenka, 2008). In addition, inactivation of VEGFR2 in neurons or trapping of endogenously released VEGF was reported to be detrimental to LTP in the hippocampus (De Rossi et al., 2016; Licht et al., 2011). Thus, we assessed the biological activity of A $\beta$  and/or VEGF on long-term synaptic plasticity in acute hippocampal slices from adult mice after theta burst stimulation (TBS) of Schaeffer collaterals. TBS failed to induce a robust LTP in A $\beta$ -treated hippocampal slices, in line with previous work (Walsh et al., 2002). In those slices, the fEPSP slope was reduced as soon as 5 min after TBS and remained impaired at 1 h after stimulation compared with that of the control slices (Figures 6A and 6B). Importantly, when VEGF was associated with A $\beta$ , TBS induced a sustained increase in the fEPSP slope, characteristic of LTP, which significantly differed from the responses obtained in A $\beta$ -treated slices (Figures 6A and

(F) VEGF induced a significant increase in averaged I/O curve slopes in *APP/PS1* slices ( $p = 0.009$ , unpaired  $t$  test,  $n = 7$ ) but not in WT slices ( $p > 0.05$ ,  $n = 7$ ).

(G and H) VEGF increased fEPSP in WT slices ( $p = 0.028$ , paired  $t$  test,  $n = 7$ ), with no change in PPF (right) (G), as in *APP/PS1* slices ( $p = 0.007$ , paired  $t$  test,  $n = 6$ ) with no change in PPF (right) (H). Inset: averaged traces before (1) and after (2) VEGF; 1+2, scaled paired-pulse responses. Scale: 1 mV, 50 ms.

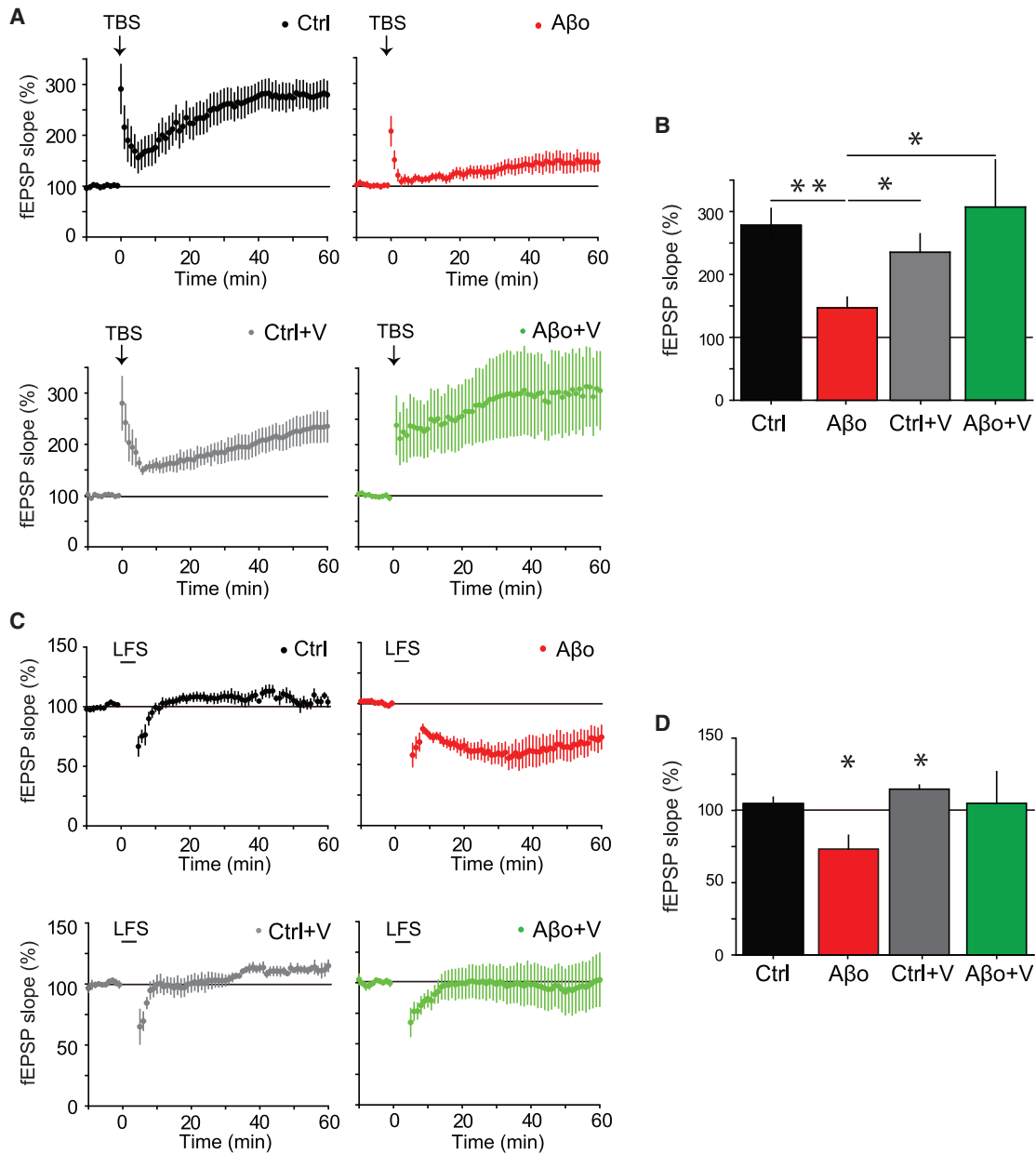


**Figure 6. VEGF rescues both LTP impairment and LTD facilitation induced by Aβ0 in the CA1 region**

(A) Time course of LTP experiments in control (black,  $n = 8$  mice), Aβ0 (red, 500 nM Aβ0,  $n = 10$ ), VEGF (gray,  $n = 6$ ), and Aβ0+VEGF (green,  $n = 9$ ) groups. (B) Means  $\pm$  SEM of LTP amplitude (at 55–60 min) for the four groups. fEPSP slope was reduced by Aβ0 (Kruskal-Wallis,  $p = 0.01$ ; post hoc  $p < 0.01$ ,  $n = 10$ –8 mice), but rescued by VEGF (post hoc  $p < 0.05$ ,  $n = 9$ –10), with no differences compared with the control (ns,  $n = 9$ –8). No further effect was observed with VEGF alone compared with that of the control (ns,  $n = 6$ –8).

(C and D) Time course of subthreshold LTD experiments in control (black), Aβ0 (red, 500 nM), VEGF (gray), and Aβ0+VEGF (green) groups. Subthreshold low-frequency stimulation (LFS, 1 Hz, 300 pulses) triggered LTD in Aβ0-treated slices but not in the control condition (55–60 min after LFS,  $p = 0.048$ , paired t test,  $n = 5$ ). In contrast, VEGF with Aβ0 prevented LTD induction (ns, paired t test,  $n = 6$ ). VEGF alone induced a small potentiation after LFS ( $p = 0.01$ , paired t test,  $n = 5$ ). \* $p < 0.05$ , \*\* $p < 0.01$ .

6B). With combined treatment, LTP reached the same level 1 h after TBS, as in the control condition (Figures 6A and 6B). Moreover, addition of VEGF alone did not further enhance TBS-induced LTP compared with the control condition (Figures 6A and 6B). Thus, we reasoned that if VEGF underlies the same

potentiation mechanism as the one occurring during LTP, VEGF should have no further potentiating effect than the one obtained in the control condition. In contrast, in Aβ0-treated slices, the resulting block of LTP would allow VEGF to strongly potentiate fEPSP responses and, therefore, to rescue LTP.

Next, we examined the VEGF impact on A $\beta$ -induced LTD facilitation in adult hippocampal slices, which is known to involve both NMDAR-dependent and NMDAR-independent forms of LTD (Shankar et al., 2008; Li et al., 2009). Importantly, A $\beta$  have been shown to induce LTD when metabotropic glutamate receptors are activated by a low-frequency subthreshold stimulation (LFS; 300 pulses at 1 Hz) (Shankar et al., 2008; Li et al., 2009). As expected, this LFS protocol triggered hippocampal LTD in A $\beta$ -treated slices, but not in the control condition, with a clear decrease in fEPSP responses compared with baseline up to 1 h after LFS (Figures 6C and 6D). In contrast, VEGF co-application with A $\beta$  prevented LTD induction (Figures 6C and 6D), highlighting VEGF blockade of A $\beta$ -induced synaptic depression.

### VEGF prevents the spine morphology alterations and loss triggered by A $\beta$

Increasing evidence has demonstrated that changes in synaptic strength involve activity-dependent structural plasticity, including remodeling of dendritic spine morphology as well as formation or removal of spines (Matsuzaki et al., 2004). Notably, synaptic dysfunction and related alteration in dendritic spine morphology and number are among the best-characterized deleterious actions of A $\beta$  (Sheng et al., 2012; Dorostkar et al., 2015). Thus, given the protective role of VEGF that we observed in A $\beta$ -induced synaptic alterations, we investigated dendritic spine remodeling in response to treatments in hippocampal neurons expressing enhanced green fluorescent protein (eGFP). We carried out a 3D quantitative analysis of dendritic spines in pyramidal neurons treated for 24 h with A $\beta$  or with a control peptide,  $\pm$  VEGF (Figure 7A). We showed that A $\beta$  triggers a significant loss of dendritic spines compared with that of the control cultures (Figures 7A and 7B), confirming previous reports (Shankar et al., 2007). Next, we investigated whether A $\beta$  affected the morphological classification of spines and observed a leftward shift in the spine head distribution toward narrower diameters, whereas spine length was not changed (Figure 7C). Mushroom as well as thin spines were selectively targeted by A $\beta$  with a resulting decrease in density (Figure 7D). Conversely, the co-application of A $\beta$  and VEGF significantly increased total spine density and reversed spine loss triggered by A $\beta$  alone (Figures 7A and 7B). This rescue effect of VEGF resulted in a morphological recovery of the dendritic spine pool, which was reflected by the rightward shift in the spine head distribution compared with the A $\beta$  condition (Figure 7C). Furthermore, we demonstrated that VEGF selectively protected mushroom spines from the deleterious action of A $\beta$ , by preventing their decrease in density (Figure 7D). Collectively, these findings strongly indicated that the VEGF effect on neurons prevents A $\beta$ -associated structural defects in dendritic spines.

### DISCUSSION

In the present study, we uncovered a crosstalk between A $\beta$  and VEGF acting directly on synapses and provided evidence for a key role for VEGF in maintaining synaptic structure and function in AD pathology.

In patients with AD, CSF levels of VEGF significantly decrease with the severity of cognitive impairment in large cohorts, mimicking A $\beta$  changes (Leung et al., 2015). That link between VEGF and A $\beta$  hallmarks raises the possibility that VEGF interacts with A $\beta$  deposits in AD brains. Such an interaction would lead to a decrease in VEGF availability in the parenchyma surrounding A $\beta$  plaques, with potential alterations linked to VEGF blockade (Licht et al., 2011; Zhang et al., 2016). In the present study, immunostaining showed that A $\beta$ <sup>+</sup> plaques were strongly labeled for VEGF in the frontal cortex of human AD brains. In contrast, VEGF expression was restricted to blood vessels in age-matched controls. This pattern of VEGF accumulation in A $\beta$  plaques was partly reproduced in young *APP/PS1* transgenic mice. These findings demonstrate that VEGF is associated with insoluble fibrillary A $\beta$  forms in both human and transgenic brain deposits, supporting previous evidence (Yang et al., 2004; Ryu et al., 2009; Thomas et al., 2015). They also suggest that VEGF is linked to the reported halo of A $\beta$  oligomers surrounding plaques (Koffie et al., 2009). Heparan sulfate proteoglycans (HSPG), known to interact with both insoluble and soluble A $\beta$  (Verbeek et al., 1999; Liu et al., 2016) and with heparin-binding VEGF isoforms (Houck et al., 1992), could provide a molecular anchor trapping those proteins in the extracellular matrix.

Previous work has demonstrated that immobilized A $\beta$  physically interacts through direct binding with the heparin-binding VEGF<sub>165</sub> isoform, leaving the diffusible VEGF<sub>121</sub> unbound (Yang et al., 2004, 2005). These VEGF isoforms differ in their binding affinity for HSPG in the extracellular matrix, which affects their diffusion properties (Ferrara et al., 2003). It has not been documented yet whether those VEGF isoforms preferentially interact with soluble A $\beta$ , known to be the main A $\beta$  pathogenic species (Serrano-Pozo et al., 2011), or with A $\beta$ m. Our biochemical analyses provided strong evidence for a selective binding of A $\beta$  to VEGF<sub>165</sub> and to a lesser extent to VEGF<sub>121</sub>, in contrast to A $\beta$ m. In addition, three major binding domains have been identified between A $\beta$  and VEGF using a peptide-array-based strategy, including the VEGFR2 binding site, common to all VEGF isoforms, and the amino-terminal part of the heparin-binding domain. Notably, these two domains are critically required for VEGF signaling. Indeed, VEGFR2 on the one hand and the interaction between HSPG and heparin-binding VEGF isoforms on the other hand can promote the formation of an active signaling complex (Selleck, 2006). Moreover, a blocking peptide targeting the amino-terminal part of the heparin binding domain has been reported to prevent VEGF<sub>165</sub> from binding the cell surface and its receptors, leading to an inhibition of its function (Lee et al., 2010b; Jia et al., 2001). Thus, the direct A $\beta$ -VEGF interaction shown in the present study further suggests a strong inhibition of VEGF-VEGFR2 signaling due to A $\beta$ . In line with those data, we documented that A $\beta$  block VEGFR2 activation in a VEGF-dependent manner in VEGFR2-expressing HEK cells and in hippocampal neurons.

Several synaptic proteins have been shown to interact with A $\beta$  and to serve as putative A $\beta$  receptors (Smith and Strittmatter 2017), some of which being immobilized by the oligomers (Renner et al., 2010). A $\beta$  ability to promote aberrant protein interaction and/or sequestration at the synapse partly underlies early synaptic deficits in AD models (Smith and Strittmatter,

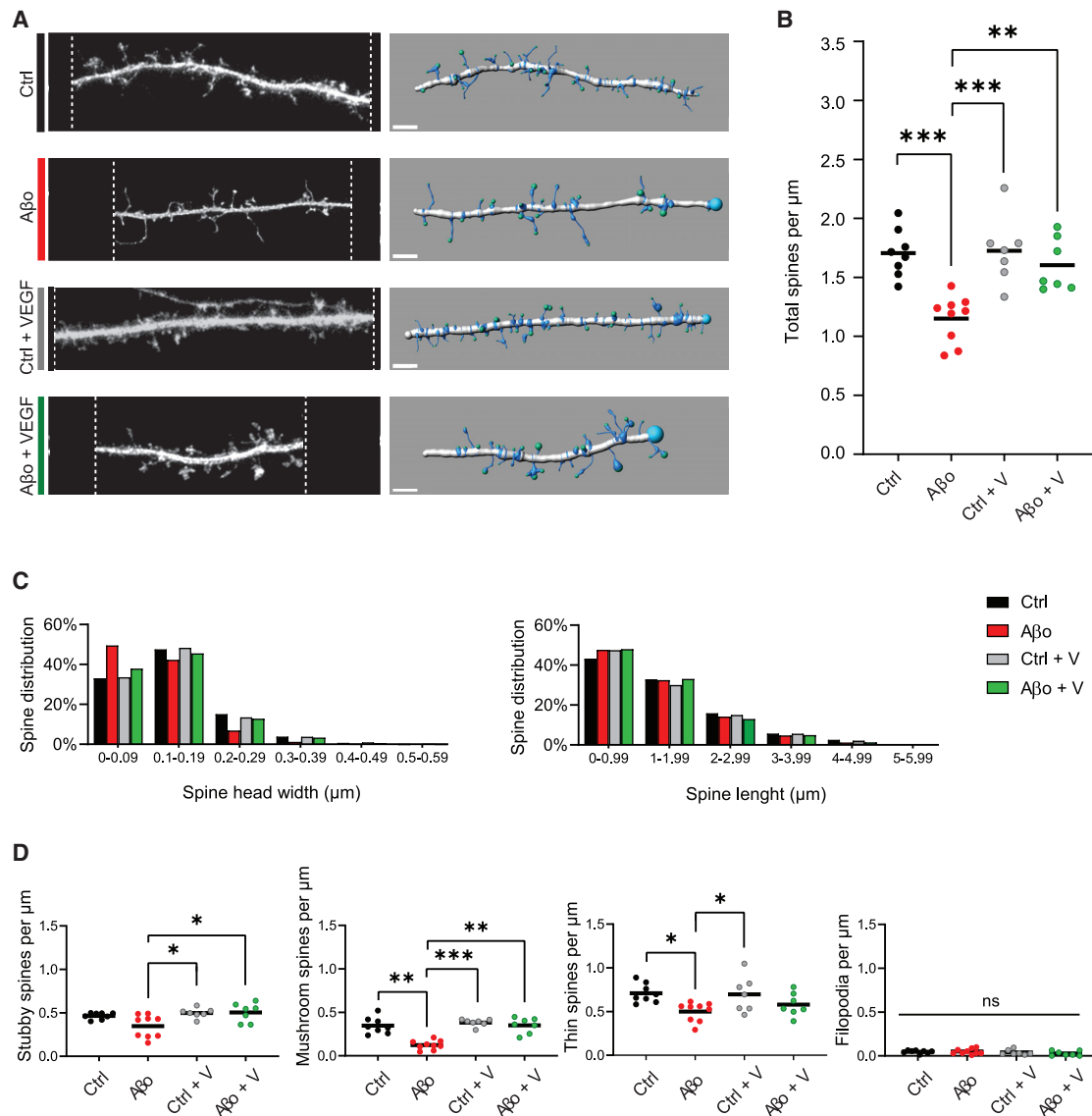


### Figure 7. VEGF prevents A $\beta$ -induced morphological alterations and loss of dendritic spines

Hippocampal neurons were transfected with eGFP on DIV 11 and treated at DIV 16–17 with control peptide (Ctrl) or A $\beta$  (500 nM),  $\pm$  50 ng  $\cdot$  mL $^{-1}$  VEGF for 1 day. (A) Representative images of dendritic segments from treated pyramidal neurons with 3D models shown in right panels. Scale bar, 2.5  $\mu\text{m}$ .

(B) Quantitative analysis showing total spine density values from  $n = 7$ –9 coverslips per condition. Spine loss triggered by A $\beta$  (one-way ANOVA,  $p < 0.0001$ ; post hoc  $p < 0.001$ ,  $n = 9$ ) was reversed by VEGF (post hoc  $p < 0.01$ ,  $n = 7$ –9).

(C) Spine head width and spine length distribution per class.

(D) Morphological classification in stubby, mushroom, thin spines, and filopodia with values indicating mean spine number per micrometer. Data were analyzed for statistical significance using a one-way ANOVA and Tukey's post hoc test or a Kruskal-Wallis and Dunn's post hoc test when ANOVA assumptions were not met (stubby, Kruskal-Wallis,  $p = 0.029$ ; mushroom, Kruskal-Wallis,  $p = 0.0003$ ; thin, one-way ANOVA,  $p = 0.0152$ ; filopodia, one-way ANOVA,  $p > 0.05$ ). A $\beta$  induced a loss of mushroom spines (post hoc  $p < 0.01$ ,  $n = 9$ –8) counteracted by VEGF (post hoc  $p < 0.01$ ,  $n = 7$ –9). \* $p < 0.05$ , \*\* $p < 0.01$ , \*\*\* $p < 0.001$ .

2017). Along those lines, our present findings indicate that A $\beta$  act as a VEGF-interacting protein that negatively regulates VEGF function in hippocampal neurons. Furthermore, we demonstrate that VEGF supplementation rescues impaired VEGFR2 activation due to A $\beta$  and compensates for A $\beta$ -induced synaptic alterations. Thus, aberrant A $\beta$ -VEGF interactions are likely to occur at synapses and to compromise VEGFR2 activation. Indeed, previous evidence documented that A $\beta$

target synapses (Lacor et al., 2004, 2007; Koffie et al., 2009) and that synaptic activity promotes the release of A $\beta$  and VEGF, respectively (Cirrito et al., 2005; Kim et al., 2008; De Rossi et al., 2016). Moreover, VEGFR2 has been shown to be expressed at hippocampal synapses, *in vitro* (De Rossi et al., 2016), as well as *in vivo* (present study). Thus, even synapses distant from A $\beta$  plaques in which VEGF is trapped may display alterations of the VEGF/VEGFR2 pathway.

In a recent study (De Rossi et al., 2016), we revealed that VEGF regulates the trafficking of surface glutamate receptors and promotes the formation of new synaptic sites. These two VEGF-dependent processes contribute to increase the pool of synapses expressing functional glutamate receptors, in sharp contrast with the reported effect of A $\beta$  on neurons. Indeed, A $\beta$  derived from synthetic or natural sources have been shown to trigger removal of surface NMDA and AMPA receptors over time, linked to the loss of synaptic sites (Snyder et al., 2005; Almeida et al., 2005). We hypothesized that the opposite actions of VEGF might rescue the decrease in synaptic glutamate receptor content induced by A $\beta$ . Because A $\beta$  produce a biphasic effect on NMDA and AMPA receptor content at synapses, with an early transient increase and a later decline (Um et al., 2012; Snyder et al., 2005; Frandemiche et al., 2014; Almeida et al., 2005), we selected a treatment duration exceeding that of the transient phase. Consistently, we found that increasing VEGF levels markedly reduced the loss of GluA1-expressing AMPAR at synapses, induced by A $\beta$ . Because AMPAR internalization depends on caspase-3 and calcineurin activation (Beattie et al., 2000; Li et al., 2010), which are causally linked (Mukerjee et al., 2000) and exacerbated in A $\beta$ -mediated pathology (D'Amelio et al., 2011), we investigated the effect of VEGF on those signaling pathways. Our biochemical findings provided strong evidence that VEGF blocks the concomitant increase in caspase-3 and calcineurin activation triggered by A $\beta$ , in line with the maintenance of AMPAR synaptic content. In addition, we demonstrated that VEGF counteracts the A $\beta$ -induced dephosphorylation of serine 845 (S845) in GluA1, which results from calcineurin activation (Miñano-Molina et al., 2011). Notably, the reversible S845 phosphorylation has a critical role in regulating AMPAR membrane insertion and function at synapses (Ehlers, 2000). Consistently, our results revealed that VEGF contributes to maintain the cell surface expression of AMPAR expressing GluA1 in the hippocampal neurons challenged by A $\beta$ . Taken together, our findings indicate that VEGF uses the same signaling hub that A $\beta$  do, which links extracellular signals to the control of AMPAR synaptic content, but with opposite effects.

Thus, VEGF may serve as a priming signal that promotes insertion of new GluA1-containing AMPAR into neuronal membrane and trafficking to synaptic sites. When synaptic transmission mediated by AMPAR is depressed by toxic A $\beta$ , we have demonstrated that VEGF partially restores synaptic strength through a postsynaptic mechanism, supporting basal synaptic transmission in this pathological context. Notably, our work highlighted the importance of VEGF for ongoing synaptic function in the *APP/PS1* mouse model of AD characterized by an age-dependent increase in A $\beta$  burden. A clear deficit in basal synaptic transmission involving postsynaptic AMPAR was observed in the CA1 region of the hippocampus in 8-month-old *APP/PS1* mice, contrary to a previous report (Gengler et al., 2010). Importantly, this deficit was partially reversed by VEGF through a postsynaptic action, illustrating the ability of VEGF to counteract the internalization of AMPAR triggered by toxic A $\beta$ , in an *in-vivo*-like environment. Interestingly, VEGF also increased basal synaptic transmission in 8-month-old WT mice, likely reflecting compensation for a previously described age-related decrease in synaptic effectiveness (Barnes et al., 2000).

Overall, these findings suggest that VEGF may have an important role in stabilizing active synapses confronted with toxic A $\beta$  signals or characterized by an age-related downregulation of synaptic transmission, raising the question of its effect in the synaptic plasticity processes.

Mechanisms underlying LTP have been shown to interact with LTD mechanisms to regulate synaptic function (Bear and Malenka, 1994). Indeed, the balance between phosphorylation and dephosphorylation of postsynaptic AMPAR is instrumental in the control of these two forms of synaptic plasticity (Lee et al., 2000, 2003). Phosphorylation of S845 may support LTP and is required for LTD (Lee et al., 2010a), with its dephosphorylation state being linked to a decrease in synaptic efficacy (Lee et al., 1998). Along that line, our results in hippocampal cultures, showing that A $\beta$  stimulate the protein phosphatase calcineurin and trigger S845 dephosphorylation, suggest that A $\beta$  alone can prime naive synapses for a decrease in synaptic efficacy. We further showed that A $\beta$  trigger a robust inhibition of LTP in the CA1 region of the hippocampus, confirming previous findings (Lambert et al., 1998; Walsh et al., 2002; Shankar et al., 2008). In addition, we demonstrated that VEGF rescues LTP inhibition triggered by A $\beta$ . Moreover, because VEGF alone fails to further increase the magnitude of LTP, we propose that its effect depends on the prior state of synapses. Therefore, in agreement with a previous study (Lee et al., 2000), we hypothesized that the S845 phosphorylation promoted by VEGF allows the potentiation of synapses that have previously been primed for depression by A $\beta$ . We observed such a priming for depression in hippocampal slices preincubated with A $\beta$  and exposed to subthreshold LFS. However, when LFS was associated with VEGF, it resulted in a rapid compensatory synaptic process that prevented synaptic depression, in support of our hypothesis. Taken together, our findings suggest that VEGF promotes the potentiation of recently depressed synapses in the adult brain with A $\beta$ -mediated pathology.

Long-term changes in synaptic plasticity are supported by morphological and structural remodeling of dendritic spines (Matsuzaki et al., 2004; Tada and Sheng 2006). In transgenic models of AD, structural alterations and loss of dendritic spines have been shown to mimic the situation observed in brain sections from patients with AD (Knafo et al., 2009; Mi et al., 2017). Those structural alterations can be reliably reproduced in hippocampal cultures or slices exposed to A $\beta$  (Shankar et al., 2007; Lacor et al., 2007). Previous studies have implicated VEGF in protecting against long-term A $\beta$ -mediated neurotoxicity in cultured neurons (Herrán et al., 2013), but its direct effect on dendritic spine loss has not previously been documented. Here, we reveal that VEGF partially rescues the changes in spine morphology induced by A $\beta$ , sparing the mushroom spines, which are considered stable-memory spines with high synaptic efficacy (Bourne and Harris, 2007; Kasai et al., 2010). Notably, this effect of VEGF results in the maintenance of dendritic spine density in hippocampal neurons challenged by A $\beta$ . Thus, the fact that VEGF counteracts mushroom spine loss and further maintains dendritic spine density highlights its functional relevance in AD pathology.

In conclusion, our findings demonstrate that VEGF can rescue early functional and structural synaptic alterations triggered by

pathogenic A $\beta$ . They further suggest a model in which A $\beta$ -VEGF binding impedes VEGF neuronal functions, whereas restoration of VEGF availability may prevent synaptic dysfunction caused by A $\beta$ .

## STAR★METHODS

Detailed methods are provided in the online version of this paper and include the following:

- **KEY RESOURCES TABLE**
- **RESOURCE AVAILABILITY**
  - Lead contact
  - Materials availability
  - Data and code availability
- **EXPERIMENTAL MODEL AND SUBJECT DETAILS**
  - Human brain sample
  - Animals
  - Mouse primary neuronal culture
  - Cell line culture
- **METHOD DETAILS**
  - A $\beta$  preparation and oligomerization
  - ELISA assays
  - Immunoprecipitation and immunoblotting
  - Electron microscopy
  - Peptide arrays
  - Electrophysiology
  - Acute hippocampal slice preparation for biochemical experiments
- **CULTURES AND TREATMENTS**
  - HEK cell transfection and treatment
  - Hippocampal neuron treatment
- **POSTSYNAPTIC DENSITY ENRICHMENT AND IMMUNOBLOTTING**
  - PSD enrichment
  - Immunoblotting
- **IMMUNOHISTOCHEMISTRY AND HIPPOCAMPAL NEURON IMMUNOSTAINING**
  - Immunohistochemistry
  - Hippocampal neuron immunostaining
  - Hippocampal neuron transfection for 3D confocal imaging
- **IMAGE ACQUISITION AND ANALYSIS**
  - Imaging of brain section and cell surface immunostainings
  - Confocal imaging of dendritic spines
  - 3D dendritic spine modeling
  - Confocal imaging of synaptic targeting
- **QUANTIFICATION AND STATISTICAL ANALYSIS**

## SUPPLEMENTAL INFORMATION

Supplemental information can be found online at <https://doi.org/10.1016/j.celrep.2021.109121>.

## ACKNOWLEDGMENTS

We thank Smatti Batoule, Annabelle Bouchardon, Bruno Chapuis, and Denis Ressnikoff from the Centre d'Imagerie Quantitative Lyon-Est; Corinne Perrin

and Anthony Terra from the CRB HCL; and Aurélie Mongope and Jean-Michel Vicat from the Animalerie Lyon-Est Module SPF facility (University Lyon 1) for assistance. We are grateful to Kevin Baranger, Anne Didier, Gilles Pages, and Laure Verret for helpful discussions. This study was supported by grants from the Institut National de la Santé et de la Recherche Médicale and the French foundations Fondation Vaincre Alzheimer (R17004CC) (to C.M.) and Fondation d'Entreprise Caisse d'Épargne Rhône-Alpes (CERA; R14154CC) (to C.M.). L.M. was supported by a doctoral research contract ADR ARC2 from the Région Rhône-Alpes, and P.B. was supported by a doctoral research contract from the French Ministry of Higher Education and Research.

## AUTHOR CONTRIBUTIONS

L.M. and P.B. contributed to the conception and study design, conducted experiments, analyzed and discussed data, and commented on the paper. N.C., C.W., and D.P. performed experiments. R.B., J.H., and A.B. discussed the data and commented on the paper, and J.H. provided financial support. D.M. provided human biopsies. P.-A.S. contributed to the study design, conducted electrophysiological experiments, analyzed and discussed data, and commented on the paper. C.M. conceptualized and supervised the study, wrote the manuscript, and provided financial support.

## DECLARATION OF INTERESTS

The authors declare no competing interests.

Received: December 19, 2019

Revised: March 4, 2021

Accepted: April 22, 2021

Published: May 11, 2021

## REFERENCES

- Alfonso, S., Kessels, H.W., Banos, C.C., Chan, T.R., Lin, E.T., Kumaravel, G., Scannevin, R.H., Rhodes, K.J., Haganir, R., Guckian, K.M., et al. (2014). Synapto-depressive effects of amyloid  $\beta$  require PICK1. *Eur. J. Neurosci.* **39**, 1225–1233.
- Almeida, C.G., Tampellini, D., Takahashi, R.H., Greengard, P., Lin, M.T., Snyder, E.M., and Gouras, G.K. (2005). Beta-amyloid accumulation in APP mutant neurons reduces PSD-95 and GluR1 in synapses. *Neurobiol. Dis.* **20**, 187–198.
- Barnes, C.A., Rao, G., and Orr, G. (2000). Age-related decrease in the Schaffer collateral-evoked EPSP in awake, freely behaving rats. *Neural Plast.* **7**, 167–178.
- Bear, M.F., and Malenka, R.C. (1994). Synaptic plasticity: LTP and LTD. *Curr. Opin. Neurobiol.* **4**, 389–399.
- Beattie, E.C., Carroll, R.C., Yu, X., Morishita, W., Yasuda, H., von Zastrow, M., and Malenka, R.C. (2000). Regulation of AMPA receptor endocytosis by a signaling mechanism shared with LTD. *Nat. Neurosci.* **3**, 1291–1300.
- Bourne, J., and Harris, K.M. (2007). Do thin spines learn to be mushroom spines that remember? *Curr. Opin. Neurobiol.* **17**, 381–386.
- Braak, H., and Braak, E. (1991). Demonstration of amyloid deposits and neurofibrillary changes in whole brain sections. *Brain Pathol.* **1**, 213–216.
- Cao, L., Jiao, X., Zuzga, D.S., Liu, Y., Fong, D.M., Young, D., and During, M.J. (2004). VEGF links hippocampal activity with neurogenesis, learning and memory. *Nat. Genet.* **36**, 827–835.
- Chiang, A.C.A., Fowler, S.W., Reddy, R., Pletnikova, O., Troncoso, J.C., Sherman, M.A., Lesne, S.E., and Jankowsky, J.L. (2018). Discrete pools of oligomeric amyloid- $\beta$  track with spatial learning deficits in a mouse model of Alzheimer amyloidosis. *Am. J. Pathol.* **188**, 739–756.
- Cirrito, J.R., Yamada, K.A., Finn, M.B., Sloviter, R.S., Bales, K.R., May, P.C., Schoepp, D.D., Paul, S.M., Mennicker, S., and Holtzman, D.M. (2005). Synaptic activity regulates interstitial fluid amyloid- $\beta$  levels in vivo. *Neuron* **48**, 913–922.

- Citri, A., and Malenka, R.C. (2008). Synaptic plasticity: multiple forms, functions, and mechanisms. *Neuropsychopharmacology* 33, 18–41.
- D'Amelio, M., Cavallucci, V., Middei, S., Marchetti, C., Pacioni, S., Ferri, A., Diamantini, A., De Zio, D., Carrara, P., Battistini, L., et al. (2011). Caspase-3 triggers early synaptic dysfunction in a mouse model of Alzheimer's disease. *Nat. Neurosci.* 14, 69–76.
- De Rossi, P., Harde, E., Dupuis, J.P., Martin, L., Chounlamountri, N., Bardin, M., Watrin, C., Benetollo, C., Pernet-Gallay, K., Luhmann, H.J., et al. (2016). A critical role for VEGF and VEGFR2 in NMDA receptor synaptic function and fear-related behavior. *Mol. Psychiatry* 21, 1768–1780.
- Diering, G.H., Heo, S., Hussain, N.K., Liu, B., and Haganir, R.L. (2016). Extensive phosphorylation of AMPA receptors in neurons. *Proc. Natl. Acad. Sci. USA* 113, E4920–E4927.
- Dorostkar, M.M., Zou, C., Blazquez-Llorca, L., and Herms, J. (2015). Analyzing dendritic spine pathology in Alzheimer's disease: problems and opportunities. *Acta Neuropathol.* 130, 1–19.
- Dubois, B., Feldman, H.H., Jacova, C., Hampel, H., Molinuevo, J.L., Blennow, K., DeKosky, S.T., Gauthier, S., Selkoe, D., Bateman, R., et al. (2014). Advancing research diagnostic criteria for Alzheimer's disease: the IWG-2 criteria. *Lancet Neurol.* 13, 614–629.
- Ehlers, M.D. (2000). Reinsertion or degradation of AMPA receptors determined by activity-dependent endocytic sorting. *Neuron* 28, 511–525.
- El Gaamouch, F., Buisson, A., Moustié, O., Lemieux, M., Labrecque, S., Bontemp, B., De Koninck, P., and Nicole, O. (2012). Interaction between  $\alpha$ CaMKII and GluN2B controls ERK-dependent plasticity. *J. Neurosci.* 32, 10767–10779.
- Esteban, J.A., Shi, S.H., Wilson, C., Nuriya, M., Haganir, R.L., and Malinow, R. (2003). PKA phosphorylation of AMPA receptor subunits controls synaptic trafficking underlying plasticity. *Nat. Neurosci.* 6, 136–143.
- Ferrara, N., Gerber, H.P., and LeCouter, J. (2003). The biology of VEGF and its receptors. *Nat. Med.* 9, 669–676.
- Frändemiche, M.L., De Seranno, S., Rush, T., Borel, E., Elie, A., Arnal, I., Lanté, F., and Buisson, A. (2014). Activity-dependent tau protein translocation to excitatory synapse is disrupted by exposure to amyloid- $\beta$  oligomers. *J. Neurosci.* 34, 6084–6097.
- García, K.O., Ornellas, F.L., Martin, P.K., Patti, C.L., Mello, L.E., Frussa-Filho, R., Han, S.W., and Longo, B.M. (2014). Therapeutic effects of the transplantation of VEGF overexpressing bone marrow mesenchymal stem cells in the hippocampus of murine model of Alzheimer's disease. *Front. Aging Neurosci.* 6, 30.
- Gengler, S., Hamilton, A., and Hölscher, C. (2010). Synaptic plasticity in the hippocampus of a APP/PS1 mouse model of Alzheimer's disease is impaired in old but not young mice. *PLoS ONE* 5, e9764.
- Haass, C., and Selkoe, D.J. (2007). Soluble protein oligomers in neurodegeneration: lessons from the Alzheimer's amyloid  $\beta$ -peptide. *Nat. Rev. Mol. Cell Biol.* 8, 101–112.
- Harde, E., Nicholson, L., Furones Cuadrado, B., Bissen, D., Wigge, S., Urban, S., Segarra, M., Ruiz de Almodóvar, C., and Acker-Palmer, A. (2019). EphrinB2 regulates VEGFR2 during dendritogenesis and hippocampal circuitry development. *eLife* 8, e49819.
- He, Y., Wei, M., Wu, Y., Qin, H., Li, W., Ma, X., Cheng, J., Ren, J., Shen, Y., Chen, Z., et al. (2019). Amyloid  $\beta$  oligomers suppress excitatory transmitter release via presynaptic depletion of phosphatidylinositol-4,5-bisphosphate. *Nat. Commun.* 10, 1193.
- Herrán, E., Pérez-González, R., Igartua, M., Pedraz, J.L., Carro, E., and Hernández, R.M. (2013). VEGF-releasing biodegradable nanospheres administered by craniotomy: a novel therapeutic approach in the APP/Ps1 mouse model of Alzheimer's disease. *J. Control. Release* 170, 111–119.
- Hohman, T.J., Bell, S.P., and Jefferson, A.L.; Alzheimer's Disease Neuroimaging Initiative (2015). The role of vascular endothelial growth factor in neurodegeneration and cognitive decline: exploring interactions with biomarkers of Alzheimer disease. *JAMA Neurol.* 72, 520–529.
- Houck, K.A., Leung, D.W., Rowland, A.M., Winer, J., and Ferrara, N. (1992). Dual regulation of vascular endothelial growth factor bioavailability by genetic and proteolytic mechanisms. *J. Biol. Chem.* 267, 26031–26037.
- Hsieh, H., Boehm, J., Sato, C., Iwatsubo, T., Tomita, T., Sisodia, S., and Malinow, R. (2006). AMPAR removal underlies A $\beta$ -induced synaptic depression and dendritic spine loss. *Neuron* 52, 831–843.
- Jarosz-Griffiths, H.H., Noble, E., Rushworth, J.V., and Hooper, N.M. (2016). Amyloid- $\beta$  receptors: the good, the bad, and the prion protein. *J. Biol. Chem.* 291, 3174–3183.
- Jia, H., Jezequel, S., Löhr, M., Shaikh, S., Davis, D., Soker, S., Selwood, D., and Zachary, I. (2001). Peptides encoded by exon 6 of VEGF inhibit endothelial cell biological responses and angiogenesis induced by VEGF. *Biochem. Biophys. Res. Commun.* 283, 164–173.
- Jin, M., and Selkoe, D.J. (2015). Systematic analysis of time-dependent neural effects of soluble amyloid  $\beta$  oligomers in culture and in vivo: prevention by scyllo-inositol. *Neurobiol. Dis.* 82, 152–163.
- Kasai, H., Hayama, T., Ishikawa, M., Watanabe, S., Yagishita, S., and Noguchi, J. (2010). Learning rules and persistence of dendritic spines. *Eur. J. Neurosci.* 32, 241–249.
- Kayed, R., Head, E., Sarsoza, F., Saing, T., Cotman, C.W., Neucula, M., Margol, L., Wu, J., Breydo, L., Thompson, J.L., et al. (2007). Fibril specific, conformation dependent antibodies recognize a generic epitope common to amyloid fibrils and fibrillar oligomers that is absent in prefibrillar oligomers. *Mol. Neurodegener.* 2, 18.
- Kim, B.W., Choi, M., Kim, Y.S., Park, H., Lee, H.R., Yun, C.O., Kim, E.J., Choi, J.S., Kim, S., Rhim, H., et al. (2008). Vascular endothelial growth factor (VEGF) signaling regulates hippocampal neurons by elevation of intracellular calcium and activation of calcium/calmodulin protein kinase II and mammalian target of rapamycin. *Cell. Signal.* 20, 714–725.
- Knafo, S., Alonso-Nanclares, L., Gonzalez-Soriano, J., Merino-Serrais, P., Fernandez-Espinosa, I., Ferrer, I., and DeFelipe, J. (2009). Widespread changes in dendritic spines in a model of Alzheimer's disease. *Cereb. Cortex* 19, 586–592.
- Koffie, R.M., Meyer-Luehmann, M., Hashimoto, T., Adams, K.W., Mielke, M.L., Garcia-Alloza, M., Micheva, K.D., Smith, S.J., Kim, M.L., Lee, V.M., et al. (2009). Oligomeric amyloid  $\beta$  associates with postsynaptic densities and correlates with excitatory synapse loss near senile plaques. *Proc. Natl. Acad. Sci. USA* 106, 4012–4017.
- Koffie, R.M., Hashimoto, T., Tai, H.C., Kay, K.R., Serrano-Pozo, A., Joyner, D., Hou, S., Kopeikina, K.J., Frosch, M.P., Lee, V.M., et al. (2012). Apolipoprotein E4 effects in Alzheimer's disease are mediated by synaptotoxic oligomeric amyloid- $\beta$ . *Brain* 135, 2155–2168.
- Lacor, P.N., Buniel, M.C., Chang, L., Fernandez, S.J., Gong, Y., Viola, K.L., Lambert, M.P., Velasco, P.T., Bigio, E.H., Finch, C.E., et al. (2004). Synaptic targeting by Alzheimer's-related amyloid  $\beta$  oligomers. *J. Neurosci.* 24, 10191–10200.
- Lacor, P.N., Buniel, M.C., Furlow, P.W., Clemente, A.S., Velasco, P.T., Wood, M., Viola, K.L., and Klein, W.L. (2007). A $\beta$  oligomer-induced aberrations in synapse composition, shape, and density provide a molecular basis for loss of connectivity in Alzheimer's disease. *J. Neurosci.* 27, 796–807.
- Lambert, M.P., Barlow, A.K., Chromy, B.A., Edwards, C., Freed, R., Liosatos, M., Morgan, T.E., Rozovsky, I., Trommer, B., Viola, K.L., et al. (1998). Diffusible, nonfibrillar ligands derived from  $\beta$ A $\beta$ 1–42 are potent central nervous system neurotoxins. *Proc. Natl. Acad. Sci. USA* 95, 6448–6453.
- Laurén, J., Gimbel, D.A., Nygaard, H.B., Gilbert, J.W., and Strittmatter, S.M. (2009). Cellular prion protein mediates impairment of synaptic plasticity by amyloid-beta oligomers. *Nature* 457, 1128–1132.
- Lee, H.K., Kameyama, K., Haganir, R.L., and Bear, M.F. (1998). NMDA induces long-term synaptic depression and dephosphorylation of the GluR1 subunit of AMPA receptors in hippocampus. *Neuron* 21, 1151–1162.
- Lee, H.K., Barbarosie, M., Kameyama, K., Bear, M.F., and Haganir, R.L. (2000). Regulation of distinct AMPA receptor phosphorylation sites during bidirectional synaptic plasticity. *Nature* 405, 955–959.

- Lee, H.K., Takamiya, K., Han, J.S., Man, H., Kim, C.H., Rumbaugh, G., Yu, S., Ding, L., He, C., Petralia, R.S., et al. (2003). Phosphorylation of the AMPA receptor GluR1 subunit is required for synaptic plasticity and retention of spatial memory. *Cell* **112**, 631–643.
- Lee, H.K., Takamiya, K., He, K., Song, L., and Huganir, R.L. (2010a). Specific roles of AMPA receptor subunit GluR1 (GluA1) phosphorylation sites in regulating synaptic plasticity in the CA1 region of hippocampus. *J. Neurophysiol.* **103**, 479–489.
- Lee, T.Y., Folkman, J., and Javaherian, K. (2010b). HSPG-binding peptide corresponding to the exon 6a-encoded domain of VEGF inhibits tumor growth by blocking angiogenesis in murine model. *PLoS ONE* **5**, e9945.
- Lesné, S., Koh, M.T., Kotilinek, L., Kaye, R., Glabe, C.G., Yang, A., Gallagher, M., and Ashe, K.H. (2006). A specific amyloid- $\beta$  protein assembly in the brain impairs memory. *Nature* **440**, 352–357.
- Leung, Y.Y., Toledo, J.B., Nefedov, A., Polikar, R., Raghavan, N., Xie, S.X., Farnum, M., Schultz, T., Baek, Y., Deerlin, V.V., et al. (2015). Identifying amyloid pathology-related cerebrospinal fluid biomarkers for Alzheimer's disease in a multicohort study. *Alzheimers Dement. (Amst.)* **1**, 339–348.
- Li, S., Hong, S., Shepardson, N.E., Walsh, D.M., Shankar, G.M., and Selkoe, D. (2009). Soluble oligomers of amyloid  $\beta$  protein facilitate hippocampal long-term depression by disrupting neuronal glutamate uptake. *Neuron* **62**, 788–801.
- Li, Z., Jo, J., Jia, J.M., Lo, S.C., Whitcomb, D.J., Jiao, S., Cho, K., and Sheng, M. (2010). Caspase-3 activation via mitochondria is required for long-term depression and AMPA receptor internalization. *Cell* **141**, 859–871.
- Licht, T., Goshen, I., Avital, A., Kreisel, T., Zubedat, S., Eavri, R., Segal, M., Yirmiya, R., and Keshet, E. (2011). Reversible modulations of neuronal plasticity by VEGF. *Proc. Natl. Acad. Sci. USA* **108**, 5081–5086.
- Liu, C.C., Zhao, N., Yamaguchi, Y., Cirrito, J.R., Kanekiyo, T., Holtzman, D.M., and Bu, G. (2016). Neuronal heparan sulfates promote amyloid pathology by modulating brain amyloid- $\beta$  clearance and aggregation in Alzheimer's disease. *Sci. Transl. Med.* **8**, 332ra44.
- Luck, R., Urban, S., Karakatsani, A., Harde, E., Sambandan, S., Nicholson, L., Haverkamp, S., Mann, R., Martin-Villalba, A., Schuman, E.M., et al. (2019). VEGF/VEGFR2 signaling regulates hippocampal axon branching during development. *eLife* **8**, e49818.
- Lue, L.F., Kuo, Y.M., Roher, A.E., Brachova, L., Shen, Y., Sue, L., Beach, T., Kurth, J.H., Rydel, R.E., and Rogers, J. (1999). Soluble amyloid  $\beta$  peptide concentration as a predictor of synaptic change in Alzheimer's disease. *Am. J. Pathol.* **155**, 853–862.
- Malinow, R. (2003). AMPA receptor trafficking and long-term potentiation. *Philos. Trans. R. Soc. Lond. B Biol. Sci.* **358**, 707–714.
- Matsuzaki, M., Honkura, N., Ellis-Davies, G.C., and Kasai, H. (2004). Structural basis of long-term potentiation in single dendritic spines. *Nature* **429**, 761–766.
- McLean, C.A., Cherny, R.A., Fraser, F.W., Fuller, S.J., Smith, M.J., Beyreuther, K., Bush, A.I., and Masters, C.L. (1999). Soluble pool of A $\beta$  amyloid as a determinant of severity of neurodegeneration in Alzheimer's disease. *Ann. Neurol.* **46**, 860–866.
- Meissirel, C., Ruiz de Almodovar, C., Knevels, E., Coulon, C., Chounlamountri, N., Segura, I., de Rossi, P., Vinckier, S., Anthonis, K., Deléglise, B., et al. (2011). VEGF modulates NMDA receptors activity in cerebellar granule cells through Src-family kinases before synapse formation. *Proc. Natl. Acad. Sci. USA* **108**, 13782–13787.
- Mi, Z., Abrahamson, E.E., Ryu, A.Y., Fish, K.N., Sweet, R.A., Mufson, E.J., and Ikonovic, M.D. (2017). Loss of precuneus dendritic spines immunopositive for spinophilin is related to cognitive impairment in early Alzheimer's disease. *Neurobiol. Aging* **55**, 159–166.
- Miñano-Molina, A.J., España, J., Martín, E., Barneda-Zahonero, B., Fadó, R., Solé, M., Trullás, R., Saura, C.A., and Rodríguez-Alvarez, J. (2011). Soluble oligomers of amyloid- $\beta$  peptide disrupt membrane trafficking of  $\alpha$ -amino-3-hydroxy-5-methylisoxazole-4-propionic acid receptor contributing to early synapse dysfunction. *J. Biol. Chem.* **286**, 27311–27321.
- Mukerjee, N., McGinnis, K.M., Park, Y.H., Gnegy, M.E., and Wang, K.K. (2000). Caspase-mediated proteolytic activation of calcineurin in thapsigargin-mediated apoptosis in SH-SY5Y neuroblastoma cells. *Arch. Biochem. Biophys.* **379**, 337–343.
- Nestor, P.J., Scheltens, P., and Hodges, J.R. (2004). Advances in the early detection of Alzheimer's disease. *Nat. Med.* **10 (Suppl)**, S34–S41.
- Oh, M.C., Derkach, V.A., Guire, E.S., and Soderling, T.R. (2006). Extrasynaptic membrane trafficking regulated by GluR1 serine 845 phosphorylation primes AMPA receptors for long-term potentiation. *J. Biol. Chem.* **281**, 752–758.
- Opazo, P., Labrecque, S., Tigaret, C.M., Frouin, A., Wiseman, P.W., De Koninck, P., and Choquet, D. (2010). CaMKII triggers the diffusional trapping of surface AMPARs through phosphorylation of stargazin. *Neuron* **67**, 239–252.
- Pickett, E.K., Koffie, R.M., Wegmann, S., Henstridge, C.M., Herrmann, A.G., Colom-Cadena, M., Leo, A., Kay, K.R., Vaught, M., Soberman, R., et al. (2016). Non-fibrillar oligomeric amyloid- $\beta$  within synapses. *J. Alzheimers Dis.* **53**, 787–800.
- Putcha, D., Brickhouse, M., O'Keefe, K., Sullivan, C., Rentz, D., Marshall, G., Dickerson, B., and Sperling, R. (2011). Hippocampal hyperactivation associated with cortical thinning in Alzheimer's disease signature regions in nondemented elderly adults. *J. Neurosci.* **31**, 17680–17688.
- Radde, R., Bolmont, T., Kaeser, S.A., Coomaraswamy, J., Lindau, D., Stoltze, L., Calhoun, M.E., Jäggi, F., Wolburg, H., Gengler, S., et al. (2006). A $\beta$ 42-driven cerebral amyloidosis in transgenic mice reveals early and robust pathology. *EMBO Rep.* **7**, 940–946.
- Religa, P., Cao, R., Religa, D., Xue, Y., Bogdanovic, N., Westaway, D., Marti, H.H., Winblad, B., and Cao, Y. (2013). VEGF significantly restores impaired memory behavior in Alzheimer's mice by improvement of vascular survival. *Sci. Rep.* **3**, 2053.
- Renner, M., Lacor, P.N., Velasco, P.T., Xu, J., Contractor, A., Klein, W.L., and Triller, A. (2010). Deleterious effects of amyloid  $\beta$  oligomers acting as an extracellular scaffold for mGluR5. *Neuron* **66**, 739–754.
- Roche, K.W., O'Brien, R.J., Mammen, A.L., Bernhardt, J., and Huganir, R.L. (1996). Characterization of multiple phosphorylation sites on the AMPA receptor GluR1 subunit. *Neuron* **16**, 1179–1188.
- Rodrigues, E.M., Scudder, S.L., Goo, M.S., and Patrick, G.N. (2016). A $\beta$ -Induced Synaptic Alterations Require the E3 Ubiquitin Ligase Nedd4-1. *J. Neurosci.* **36**, 1590–1595.
- Ryu, J.K., Cho, T., Choi, H.B., Wang, Y.T., and McLarnon, J.G. (2009). Microglial VEGF receptor response is an integral chemotactic component in Alzheimer's disease pathology. *J. Neurosci.* **29**, 3–13.
- Salter, M.W., and Kalia, L.V. (2004). Src kinases: a hub for NMDA receptor regulation. *Nat. Rev. Neurosci.* **5**, 317–328.
- Selleck, S.B. (2006). Signaling from across the way: transactivation of VEGF receptors by HSPGs. *Mol. Cell* **22**, 431–432.
- Serrano-Pozo, A., Frosch, M.P., Masliah, E., and Hyman, B.T. (2011). Neuropathological alterations in Alzheimer disease. *Cold Spring Harb. Perspect. Med.* **1**, a006189.
- Shankar, G.M., Bloodgood, B.L., Townsend, M., Walsh, D.M., Selkoe, D.J., and Sabatini, B.L. (2007). Natural oligomers of the Alzheimer amyloid- $\beta$  protein induce reversible synapse loss by modulating an NMDA-type glutamate receptor-dependent signaling pathway. *J. Neurosci.* **27**, 2866–2875.
- Shankar, G.M., Li, S., Mehta, T.H., Garcia-Munoz, A., Shepardson, N.E., Smith, I., Brett, F.M., Farrell, M.A., Rowan, M.J., Lemere, C.A., et al. (2008). Amyloid- $\beta$  protein dimers isolated directly from Alzheimer's brains impair synaptic plasticity and memory. *Nat. Med.* **14**, 837–842.
- Sheng, M., Sabatini, B.L., and Südhof, T.C. (2012). Synapses and Alzheimer's disease. *Cold Spring Harb. Perspect. Biol.* **4**, a005777.
- Smith, L.M., and Strittmatter, S.M. (2017). Binding sites for amyloid- $\beta$  oligomers and synaptic toxicity. *Cold Spring Harb. Perspect. Med.* **7**, a024075.
- Snyder, E.M., Nong, Y., Almeida, C.G., Paul, S., Moran, T., Choi, E.Y., Nairn, A.C., Salter, M.W., Lombroso, P.J., Gouras, G.K., and Greengard, P. (2005). Regulation of NMDA receptor trafficking by amyloid- $\beta$ . *Nat. Neurosci.* **8**, 1051–1058.

- Stine, W.B., Jr., Dahlgren, K.N., Krafft, G.A., and LaDu, M.J. (2003). In vitro characterization of conditions for amyloid- $\beta$  peptide oligomerization and fibrillogenesis. *J. Biol. Chem.* *278*, 11612–11622.
- Tada, T., and Sheng, M. (2006). Molecular mechanisms of dendritic spine morphogenesis. *Curr. Opin. Neurobiol.* *16*, 95–101.
- Thal, D.R., Rüb, U., Orantes, M., and Braak, H. (2002). Phases of A $\beta$ -deposition in the human brain and its relevance for the development of AD. *Neurology* *58*, 1791–1800.
- Thomas, T., Miners, S., and Love, S. (2015). Post-mortem assessment of hypoperfusion of cerebral cortex in Alzheimer's disease and vascular dementia. *Brain* *138*, 1059–1069.
- Ting, J.T., Kelley, B.G., Lambert, T.J., Cook, D.G., and Sullivan, J.M. (2007). Amyloid precursor protein overexpression depresses excitatory transmission through both presynaptic and postsynaptic mechanisms. *Proc. Natl. Acad. Sci. USA* *104*, 353–358.
- Ulrich, J.D., Finn, M.B., Wang, Y., Shen, A., Mahan, T.E., Jiang, H., Stewart, F.R., Piccio, L., Colonna, M., and Holtzman, D.M. (2014). Altered microglial response to A $\beta$  plaques in APPPS1-21 mice heterozygous for TREM2. *Mol. Neurodegener.* *9*, 20.
- Um, J.W., Nygaard, H.B., Heiss, J.K., Kostylev, M.A., Stagi, M., Vortmeyer, A., Wisniewski, T., Gunther, E.C., and Strittmatter, S.M. (2012). Alzheimer amyloid- $\beta$  oligomer bound to postsynaptic prion protein activates Fyn to impair neurons. *Nat. Neurosci.* *15*, 1227–1235.
- Verbeek, M.M., Otte-Höller, I., van den Born, J., van den Heuvel, L.P., David, G., Wesseling, P., and de Waal, R.M. (1999). Agrin is a major heparan sulfate proteoglycan accumulating in Alzheimer's disease brain. *Am. J. Pathol.* *155*, 2115–2125.
- Viola, K.L., and Klein, W.L. (2015). Amyloid  $\beta$  oligomers in Alzheimer's disease pathogenesis, treatment, and diagnosis. *Acta Neuropathol.* *129*, 183–206.
- Walsh, D.M., Klyubin, I., Fadeeva, J.V., Cullen, W.K., Anwyl, R., Wolfe, M.S., Rowan, M.J., and Selkoe, D.J. (2002). Naturally secreted oligomers of amyloid  $\beta$  protein potently inhibit hippocampal long-term potentiation in vivo. *Nature* *416*, 535–539.
- Winblad, B., Amouyel, P., Andrieu, S., Ballard, C., Brayne, C., Brodaty, H., Cedazo-Minguez, A., Dubois, B., Edvardsson, D., Feldman, H., et al. (2016). Defeating Alzheimer's disease and other dementias: a priority for European science and society. *Lancet Neurol.* *15*, 455–532.
- Yang, S.P., Bae, D.G., Kang, H.J., Gwag, B.J., Gho, Y.S., and Chae, C.B. (2004). Co-accumulation of vascular endothelial growth factor with  $\beta$ -amyloid in the brain of patients with Alzheimer's disease. *Neurobiol. Aging* *25*, 283–290.
- Yang, S.P., Kwon, B.O., Gho, Y.S., and Chae, C.B. (2005). Specific interaction of VEGF165 with  $\beta$ -amyloid, and its protective effect on  $\beta$ -amyloid-induced neurotoxicity. *J. Neurochem.* *93*, 118–127.
- Zhang, Y., Yang, Y., Hosaka, K., Huang, G., Zang, J., Chen, F., Zhang, Y., Samani, N.J., and Cao, Y. (2016). Endocrine vasculatures are preferable targets of an antitumor ineffective low dose of anti-VEGF therapy. *Proc. Natl. Acad. Sci. USA* *113*, 4158–4163.
- Zhao, W.Q., Santini, F., Breese, R., Ross, D., Zhang, X.D., Stone, D.J., Ferrer, M., Townsend, M., Wolfe, A.L., Seager, M.A., et al. (2010). Inhibition of calcineurin-mediated endocytosis and alpha-amino-3-hydroxy-5-methyl-4-isoxazolepropionic acid (AMPA) receptors prevents amyloid  $\beta$  oligomer-induced synaptic disruption. *J. Biol. Chem.* *285*, 7619–7632.

## STAR★METHODS

### KEY RESOURCES TABLE

REAGENT or RESOURCE	SOURCE	IDENTIFIER
<b>Antibodies</b>		
Mouse Anti $\beta$ -Amyloid 1-16 monoclonal antibody Dilution 1:500	BioLegend	Cat# 8003002; RRID: AB_2564654
Mouse Anti $\beta$ -Amyloid 1-16 monoclonal antibody 4 $\mu$ g for IP	BioLegend	Cat# 8003002; RRID: AB_2564654
Rabbit Anti biotin polyclonal antibody Dilution 1:10,000	Abcam	Cat# Ab53494; RRID: AB_867860
Mouse Anti HA monoclonal antibody 4 $\mu$ g for IP	Sigma-Aldrich	Cat# H3663; RRID: AB_262051
Rabbit Anti GluR1 monoclonal antibody Dilution 1:500	Millipore	Cat# 04-855; RRID: AB_1977216
Rabbit Anti phospho GluR1, (Ser845) polyclonal antibody Dilution 1:500	Millipore	Cat# Ab5849; RRID: AB_92079
Rabbit Anti phospho GluR1, (Ser831) monoclonal antibody Dilution 1:500	Millipore	Cat# 04-823; RRID: AB_1977218
Mouse Anti NR1 monoclonal antibody Dilution 1:500	Millipore	Cat# 05-432; RRID: AB_390129
Mouse Anti CaMKII monoclonal antibody Dilution 1:10,000	Abcam	Cat# Ab22609; RRID: AB_447192
Rabbit Anti phospho CaMKII $\alpha$ (Thr286) polyclonal antibody Dilution 1:500	Abcam	Cat# Ab5683; RRID: AB_305050
Rabbit Anti Fyn polyclonal antibody Dilution 1:1000	Cell Signaling Technology	Cat# 4023; RRID: AB_10698604
Rabbit Anti phospho Src Family (Tyr416) polyclonal antibody Dilution 1:1000	Cell Signaling Technology	Cat# 2101; RRID: AB_331697
Rabbit Anti Calcineurin A polyclonal antibody Dilution 1:1000	Abcam	Cat# Ab3673; RRID: AB_303991
Rabbit Anti Caspase 3 polyclonal antibody Dilution 1:1000	Cell Signaling Technology	Cat# 9662; RRID: AB_331439
Rabbit Anti Cleaved Caspase 3 polyclonal antibody Dilution 1:500	Cell Signaling Technology	Cat# 9661; RRID: AB_2341188
Rabbit Anti PSD95 monoclonal antibody Dilution 1:1000	Cell Signaling Technology	Cat# 3450; RRID: AB_2292883
Mouse Anti Synaptophysin monoclonal antibody Dilution 1:10,000	Millipore	Cat# MAB368; RRID: AB_94947
Mouse Anti $\beta$ -Actin monoclonal antibody Dilution 1:40,000	Sigma-Aldrich	Cat# A1978; RRID: AB_476692
Rabbit Anti VEGF Receptor 2 monoclonal antibody Dilution 1:500-1000	Cell Signaling Technology	Cat# 2479; RRID: AB_2212507
Rabbit Anti VEGF Receptor 2 phospho (Tyr1175) monoclonal antibody Dilution 1:250	Cell Signaling Technology	Cat# 2478; RRID: AB_331377
Goat Anti Rabbit HRP polyclonal antibody Dilution 1:10,000	Jackson Immunoresearch	Cat# 111-036-003; RRID: AB_2337942
Goat Anti mouse HRP polyclonal antibody Dilution 1:10,000	Jackson Immunoresearch	Cat# 115-036-003; RRID: AB_2338518
Rabbit Anti rat GluR1 polyclonal antibody Dilution 1:60	Millipore	Cat# PC246; RRID: AB_564636

(Continued on next page)

REAGENT or RESOURCE	SOURCE	IDENTIFIER
Rabbit Anti eGFP polyclonal antibody Dilution 1:1000	Millipore	Cat# Ab3080; RRID: AB_91337
Rabbit Anti Alexa fluor 488 polyclonal antibody Dilution 1:1000	Molecular Probes	Cat# A-11094; RRID: AB_221544
Mouse Anti $\beta$ -Amyloid 17-24 monoclonal antibody Dilution 1:500	BioLegend	Cat# 800710; RRID: AB_2565326
Rabbit Anti VEGF polyclonal antibody Dilution 1:200	Santa Cruz	Cat# sc-152; RRID: AB_2212984
Rabbit Anti OC polyclonal antibody Dilution 1:500	Millipore	Cat# Ab2286; RRID: AB_1977024
Mouse Anti GFAP monoclonal antibody Dilution 1:500	Sigma Aldrich	Cat# G3893; RRID: AB_477010
Mouse Anti CD68 monoclonal antibody Dilution 1:100	Bio-Rad	Cat# MCA1957; RRID: AB_322219
Goat Anti Mouse Alexa fluor 488 polyclonal antibody Dilution 1:1000	Molecular Probes	Cat# A11029; RRID: AB_138404
Goat Anti Rabbit Alexa fluor 555 polyclonal antibody Dilution 1:1000 – 1:100 (saturating concentration)	Molecular Probes	Cat# A21429; RRID: AB_2535850
Goat Anti Mouse Alexa fluor 647 polyclonal antibody Dilution 1:1000	Molecular Probes	Cat# A21236; RRID: AB_2535805
<b>Biological samples</b>		
Postmortem human brain tissue samples See <a href="#">Table S1</a> for more information	Hospices Civils Lyon Centre de Pathologie Neuropathologie Est	Cardiobiotec and Neurobiotec bank
<b>Chemicals, peptides, and recombinant proteins</b>		
Amyloid $\beta$ -Protein (1-42)	Bachem	Cat# H-1368
Biotinyl-Amyloid $\beta$ -Protein (1-40)	Bachem	Cat# H-5914
Biotinyl-Amyloid $\beta$ -Protein (1-42)	Bachem	Cat# H-5642
Amyloid $\beta$ -Protein (1-42) (scrambled)	Bachem	Cat# H-7406
Recombinant Human VEGF 165	R&D Systems	Cat# 293-VE
Recombinant Human VEGF 121	R&D Systems	Cat# 4644-VS
Recombinant Human VEGF 165A protein -Biotin	Abcam	Cat# ab168684
<b>Critical commercial assays</b>		
Human VEGF DuoSet ELISA	R&D Systems	Cat# DY293B
Dynabeads™ Protein G Immunoprecipitation Kit	ThermoFisher scientific	Cat# 10007D
DynaM™-2 Magnet	ThermoFisher scientific	Cat# 12321D
<b>Experimental models: Cell lines</b>		
HEK293 cells (human embryonic kidney cells)	ATCC	Cat# CRL-1573; RRID: CVCL_0045
<b>Experimental models: Organisms/strains</b>		
APP/PS1-21 Transgenic mice	<a href="#">Radde et al., 2006</a>	N/A
C57BL/6Jrj	Janvier Labs	Cat# SC-C57J-F
<b>Recombinant DNA</b>		
Plasmid: pFlk1 (VEGFR2)	<a href="#">Meissirel et al., 2011</a>	N/A
Plasmid: pEGFP-C1	Clontech	N/A
<b>Software and algorithms</b>		
Fiji – ImageJ	McMaster Biophotonics Facility	Version 1.51r
Huygens	Scientific Volume Imaging	Version 16.05

(Continued on next page)

**Continued**

REAGENT or RESOURCE	SOURCE	IDENTIFIER
Icy Bioimage Analysis Spot Detector plugin Colocalization studio plugin	France Bioimaging	Version 2.0.0.0
Imaris Spine classification MATLAB Plugin (see <a href="#">Method details</a> )	Bitplane	Version 7.6.5
Prism	GraphPad	Version 7.00
R software	R Foundation for Statistical Computing	R version 4.0.3
Origin Lab	Origin Lab Corp.	OriginPro version 2020
<b>Other</b>		
Neurobasal Medium	ThermoFisher Scientific	Cat# 21103049
B27 Supplement	ThermoFisher Scientific	Cat# 17504044
DMEM high glucose, pyruvate	ThermoFisher Scientific	Cat# 41966029
Streptavidin-HRP	R&D Systems	Cat# DY998
cOMplete protease inhibitor cocktail	Roche	Cat# 04693159001
12% Criterion™ TGX Stain-Free Protein gel	Bio-Rad	Cat# 5678044
4–12% Criterion XT Bis-Tris Protein Gel	Bio-Rad	Cat# 3450124
SuperSigna West Pico PLUS Chemiluminescent Substrate	ThermoFisher Scientific	Cat# 34577
Picrotoxin	Sigma-Aldrich	Cat# P1675
NBQX	Tocris	Cat# 1044
Tetraethylammonium chloride	Sigma-Aldrich	Cat# T2265
Sodium orthovanadate	Biolabs	Cat# P0758S
Phosphatase inhibitor cocktail	Merck Millipore	Cat# 524629
OptiMEM	ThermoFisher Scientific	Cat# 31985070
Lipofectamine LTX Reagent with PLUS Reagent	ThermoFisher Scientific	Cat# 15338100
Pierce Universal Nuclease for Cell Lysis	ThermoFisher Scientific	Cat# 88701
D-PBS no calcium no magnesium	ThermoFisher Scientific	Cat# 14190250
Thioflavin-S	Sigma Aldrich	Cat# T1892
Sudan Black B	Sigma-Aldrich	Cat# 199664
DAPI	Roche	Cat# 10236276001
FluorSave™ reagent	Merck Millipore	Cat# 345789
Alexa fluor 546 Phalloidin	ThermoFisher Scientific	Cat# A22283
Cellulose-bound peptide arrays - Celluspot	Proteomic Solutions	N/A
Extracellular amplifier	WPI	Cat# SYS-DAM80

**RESOURCE AVAILABILITY**

**Lead contact**

Further information and requests for resources and reagents should be directed to and will be fulfilled by the lead contact, Claire Meissirel ([claire.meissirel@inserm.fr](mailto:claire.meissirel@inserm.fr)).

**Materials availability**

This study did not generate new unique reagents. All key resources are listed in [Key resources table](#). Further information and requests for resources and reagents should be directed to the lead contact.

**Data and code availability**

This study did not generate and/or analyze datasets or code. All data are included in this published article and supplementary information.

## EXPERIMENTAL MODEL AND SUBJECT DETAILS

### Human brain sample

Postmortem tissue samples were obtained from the F2 region of the premotor cortex of 4 clinically and pathologically diagnosed Alzheimer's disease patients and 4 control cases. The median age of these patients was 55-year-old, 7 were females and 1 was male (Table S1). After pathological review, each postmortem specimen was assigned a Braak score based on neuronal neurofibrillary tangle pathology (Braak and Braak, 1991) and a Thal score based on amyloid deposits (Thal et al., 2002). Cases with long post-mortem intervals were excluded due to potential protein degradation with increasing post-mortem intervals. Frozen brain tissues were acquired from Hospices Civils de Lyon, Centre de Pathologie et Neuropathologie Est, Cardiobiotec and Neurobiotec bank (Lyon, France) in compliance with French ethical rules.

### Animals

Embryonic day 17-18 (E17-18) C57BL/6Jrj wild-type male and female mice were used for primary hippocampal cell cultures, biochemical purification experiments and immunostainings. In addition, brain section immunostainings, tissue fractionation and electrophysiological experiments were performed on 4 and 8-month-old wild-type and transgenic heterozygous male *APP/PS1-21* mice generated on a C57BL/6 background and expressing a transgene combining human *APP* with the Swedish mutation (*APP*<sup>KM670/671NL</sup>) and mutated *L166P* human presenilin 1 (*PS1*) under the *Thy1* promoter (Radde et al., 2006). Genotyping was performed to reveal the presence or absence of *APP* and *PS1* transgenes. For electrophysiological field potential recordings C57BL/6Jrj wild-type (P40-P70) female mice were also used. The study was conducted in accordance with the European Community Council directive 2010/63/EU on the protection of animals used for experimental and scientific purposes. Animal care and treatment procedures were performed according to the guidelines approved by the French Ethical Committee of the Lyon 1 University (DR2013-47).

### Mouse primary neuronal culture

Primary hippocampal neuron cultures were prepared from E17-18 C57BL/6Jrj mice. Briefly, hippocampi were removed, cut into pieces, digested in trypsin (0.5% w/v) and DNase (0.01% w/v) and triturated in Neurobasal medium supplemented with L-glutamine (2 mM), 2% B27, 1% penicillin-streptomycin (10000 U/mL) and D-Glucose (0.65 mg/mL). Hippocampal neurons were then plated onto poly-L-lysine coated coverslips or dishes at either low ( $19 \times 10^3$  cells/cm<sup>2</sup>) or high density ( $50 \times 10^3$  cells/cm<sup>2</sup>), depending on experiments (Table S2). Neurons were subsequently cultured in supplemented Neurobasal medium at 37°C under 5% CO<sub>2</sub>, one-half of the media changed twice a week.

### Cell line culture

HEK293 cells (human embryonic kidney cells) were routinely cultured in 6cm Petri dishes with 5mL of DMEM supplemented with 10% SVF and 100U/ml Penicillin/streptomycin.

## METHOD DETAILS

### A $\beta$ preparation and oligomerization

Synthetic A $\beta$ <sub>1-42</sub>, A $\beta$ <sub>1-40</sub>, their biotinylated forms and scrambled peptides were obtained as lyophilized samples from Bachem (A $\beta$ <sub>1-42</sub>, b-A $\beta$ <sub>1-40</sub>, b-A $\beta$ <sub>1-42</sub>, scrambled A $\beta$ <sub>1-42</sub>). Briefly, peptides were solubilized in 1,1,1,3,3,3-hexafluoro-2-propanol to prevent oligomerization, then evaporated overnight under a chemical fume hood, and stored as a dried peptide film at -80°C until use, as previously described (Stine et al., 2003). A $\beta$  oligomers were prepared extemporaneously by first dissolving the peptide film in 2 mM dimethyl sulfoxide with an additional dilution step to 100  $\mu$ M in ice-cold medium depending on experiments (Neurobasal, PBS or ACSF). Diluted peptides were subsequently incubated 24h at 4°C to form oligomers (A $\beta$ o), whereas monomers (A $\beta$ m) were directly used after the dilution step. For treatments, solutions of 100  $\mu$ M A $\beta$ o, A $\beta$ m or scrambled peptides were diluted in fresh appropriate medium to a final concentration of 500 nM for electrophysiological and morphological experiments or to 500 nM or 1  $\mu$ M for biochemical and immunohistochemical experiments. A $\beta$ o concentrations are corresponding to monomer equivalent concentrations, as previously reported (Laurén et al., 2009).

### ELISA assays

Human VEGF DuoSet ELISA assays were purchased from R&D Systems to analyze binding between recombinant human VEGF<sub>121</sub> or VEGF<sub>165</sub> and synthetic biotinylated A $\beta$ <sub>1-42</sub> oligomers or A $\beta$ <sub>1-40</sub> monomers. Binding was determined using an indirect ELISA in which VEGF was used as the capture antigen and biotinylated A $\beta$  for the detection. Briefly, 96 well plates were coated with 500 ng.mL<sup>-1</sup> of VEGF<sub>165</sub> or VEGF<sub>121</sub> in PBS. After a washing step in PBS 0.05% Tween 20, plates were blocked with 3% BSA in PBS for 1h at RT. A $\beta$  samples were added in triplicate from 0.1  $\mu$ g.mL<sup>-1</sup> to 50  $\mu$ g.mL<sup>-1</sup> (21 nM to 10.5  $\mu$ M for A $\beta$ <sub>1-42</sub>, 22 nM to 11  $\mu$ M for A $\beta$ <sub>1-40</sub>) and incubated for 2h at RT, washed with PBS 0.05% Tween 20 and subsequently incubated with HRP-conjugated streptavidin (1/40) for 20 min at RT. After washing, substrate solution containing 3,3',5,5'-Tetramethylbenzidine (TMB) and H<sub>2</sub>O<sub>2</sub> was added to the wells and reaction was stopped by H<sub>2</sub>SO<sub>4</sub>. Absorbance was successively measured at 450 and 540 nm with a TECAN microplate

reader and optical density values at 540 nm were subtracted from the ones at 450 nm to correct for optical imperfections of the plate. Unspecific A $\beta$  binding was determined using non-coated wells.

### Immunoprecipitation and immunoblotting

For immunoprecipitation, 450 ng of A $\beta$ <sub>1-42</sub> oligomer preparation were subjected to an additional overnight incubation at RT. These samples corresponding to 500 nM equivalent monomer concentration were incubated for 1 h at RT in presence or absence of 1,25 nM biotinylated VEGF<sub>165</sub> with a cOmplete protease inhibitor cocktail. Subsequently, they were incubated 2 h at 4°C with a mouse anti-A $\beta$  (4  $\mu$ g, 6E10) or control antibody (4  $\mu$ g, mouse anti-HA). Immunoprecipitates were then incubated with protein G-conjugated magnetic beads for 2 h at 4°C and selectively isolated using a magnet. After extensive washing of the magnetic beads in buffer, immunoprecipitates were eluted at RT using ammonium hydroxide 150 mM pH, 10.5 and eluates were diluted in sample buffer without DTT prior to immunoblotting analysis. Samples were separated on 12% SDS/PAGE gels, transferred on nitrocellulose membranes and immunoblotted with the antibody of interest: mouse anti-A $\beta$  (6E10) or rabbit anti-biotin.

### Electron microscopy

Prior to imaging, 5  $\mu$ L of A $\beta$ <sub>1-42</sub> oligomeric preparation at 15  $\mu$ M were deposited onto Formvar-coated mesh copper grids. After a 2 min incubation step at RT, grids were rinsed with sterile dH<sub>2</sub>O. Samples were subsequently stained using 2% uranyl acetate for 1 minute in the dark to increase contrast and were allowed to air dry for 2 minutes. Finally, they were visualized with a Philips EM208 Transmission Electron Microscope operating at 120 kV, initially imaged at low magnification (20,000X), and thereafter at 120,000X using a Gatan Orius 600 digital camera.

### Peptide arrays

Cellulose-bound peptide arrays encompassing the whole human (UniProtKB #P15692) and mouse (UniProtKB #Q00731) VEGF sequences, minus signal sequences, were synthesized by Proteomic Solutions. Overlapping 15-mer peptides were shifted by 6 aa for both human and murine sequences and two copies of the same array were spotted on the slide for quality control and reproducibility. Arrays were blocked for 2 h in Tris buffered saline, 1% Tween 20, 5% BSA to prevent unspecific binding, and subsequently probed for 15 h at 4°C with biotinylated A $\beta$ <sub>1-42</sub> oligomers (10  $\mu$ g.mL<sup>-1</sup> – 2.11  $\mu$ M), biotinylated A $\beta$ <sub>1-40</sub> monomers (10  $\mu$ g.mL<sup>-1</sup> – 2.19  $\mu$ M), or vehicle used as a control. Synthetic A $\beta$ <sub>1-40</sub> monomers were used as controls instead of A $\beta$ <sub>1-42</sub> due to aggregation properties of A $\beta$ <sub>1-42</sub> over time. After washing in TBS 1% Tween 20, arrays were incubated with HRP-conjugated Streptavidin for 2 h at RT. Peptide interaction was detected using SuperSigna West Pico PLUS Chemiluminescent Substrate according to the manufacturer's instructions. Non-specific A $\beta$  binding was determined using control peptides. Spots were quantified using ImageJ software and OD values measured with control incubation assigned as background. For each experiment, OD values reflecting binding to the duplicated spots were used to calculate the mean value for each spot.

### Electrophysiology

Local field potential recordings (LFP) were performed on acute coronal hippocampal slices from wild-type C57BL/6JRj female mice (P40-70) and 8-month-old wild-type and transgenic heterozygous male APP/PS1-21 mice to measure baseline synaptic response, long-term potentiation (LTP) and long-term depression (LTD) of Schaffer collaterals to CA1 pyramidal cell synapses (SC-CA1 synapses), (Table S2). Hippocampal slices (400  $\mu$ m thick) were cut using a vibratome (Leica VT1000S and VT1200S) and incubated at room temperature in artificial cerebrospinal fluid (ACSF) containing (in mM): 124 NaCl, 10 glucose, 1.25 NaH<sub>2</sub>PO<sub>4</sub>, 2.5 KCl, 26 NaHCO<sub>3</sub>, 1.3 MgCl<sub>2</sub>, and 2.5 CaCl<sub>2</sub>, bubbled with 95% O<sub>2</sub> and 5% CO<sub>2</sub>, pH 7.4) for 1 h prior to recording. Field extracellular excitatory post-synaptic potentials (fEPSPs) were recorded in stratum radiatum of CA1 region in presence of gamma-aminobutyric acid (GABA)-A receptor antagonist picrotoxin (100  $\mu$ M). Electrical stimulation was realized with a bipolar tungsten electrode placed in stratum radiatum and fEPSPs were measured using borosilicate glass microelectrodes (~1-3 M $\Omega$ ) filled with NaCl (1 M), or ACSF. The tip of the recording electrode was located close to the slice surface. LFP were amplified and low-pass filtered at 3 kHz using a differential amplifier. Data acquisition and analyses were carried out using a National Instrument interface coupled with Elphy software (G. Sadoc, UNIC-CNRS, Gif-sur-Yvette, France). LFP were sampled at 10 kHz. We computed fEPSPs initial slope to quantify synaptic responses. After baseline recordings of synaptic activity evoked at 0.2 Hz for at least 10 minutes, slices were treated with A $\beta$  (500 nM) or vehicle for 40 min before LTP or LTD induction. To minimize indirect effects, local VEGF applications (500 ng.mL<sup>-1</sup>) were subsequently performed using a Picospritzer II (Pulse 0.1 Hz; 50ms duration) and a glass pipette (10  $\mu$ m aperture) located in the vicinity of the recording electrode slightly above the slice surface, 15-20 min before inducing LTP and LTD (De Rossi et al., 2016). Input/output (I/O) curves were assessed by progressively raising the stimulation intensity from 20 to 400  $\mu$ A. The AMPA-R antagonist 2,3-Dioxo-6-nitro-1,2,3,4-tetrahydrobenzo[f]quinoxaline-7-sulfonamide disodium salt (NBQX, 5 $\mu$ M) was applied at the end of several experiments, after long-term application of A $\beta$  and/or VEGF to assess the fiber volley amplitude. In all experiments, NBQX totally blocked fEPSP but not the fiber volleys (Figure 5C). For assessing basal synaptic transmission, paired-pulse facilitation (PPF) was obtained by applying two electrical stimulations separated by 50ms. PPF was then analyzed by calculating the ratio of the slope of the second response to the slope of the first. A change in PPF is indicative of a (presynaptic) modulation of the probability of glutamate release at the SC-CA1 synapse. LTP was induced by a theta burst stimulation (TBS), which consisted of 10 trains separated by 30 s, each train composed of 6 bursts at 5 Hz and each burst providing 4 pulses at 100Hz. Subthreshold low-frequency

stimulus (LFS) consisted of a stimulation of 300 pulses at 1 Hz and was done in the absence of picrotoxin in ACSF (Shankar et al., 2008; Li et al., 2009). Before LTP and LTD induction, precautions were taken to ensure that approximately the same amplitude of fEPSPs was obtained in baseline for the different experiments to achieve the same level of cooperativity in each group. After LTP induction, fEPSPs were recorded for at least 60 min.

### Acute hippocampal slice preparation for biochemical experiments

Acute coronal slices (150  $\mu$ m thick) were prepared from wild-type C57BL/6Jrj female mice (P40–70) with a vibratome and incubated at room temperature in oxygenated (95% O<sub>2</sub> / 5% CO<sub>2</sub>) ACSF (in mM): 124 NaCl, 10 glucose, 1.25 NaH<sub>2</sub>PO<sub>4</sub>, 2.5 KCl, 26 NaHCO<sub>3</sub>, 1.3 MgCl<sub>2</sub>, and 2.5 CaCl<sub>2</sub>, pH 7.4, after hippocampus isolation. Next, hippocampal slices were pretreated for 40 minutes in oxygenated ACSF with 500 nM A $\beta$   $\pm$  VEGF prior to cLTP induction with 25 mM tetraethylammonium chloride (TEA) for 10 minutes. After cLTP induction, slices were maintained in initial treatments for 60 minutes and collected in cold lysis buffer (mM): 50 Tris-HCL, 150 NaCl, 1 EDTA, 1% NP-40, 0.5% deoxycholate, 0.1% SDS, supplemented with a cOmplete protease inhibitor cocktail, 2mM Sodium orthovanadate, and a phosphatase inhibitor cocktail at pH 7.4. Subsequently, hippocampal tissue was homogenized, Potterized and centrifuged at 1000 g for 10 min at 4°C and supernatants were kept at –20°C until use.

## CULTURES AND TREATMENTS

### HEK cell transfection and treatment

Cell transfection was performed at 50% confluency in DMEM supplemented with 10% SVF. A transfection medium was prepared with 237  $\mu$ L of OptiMEM, 3.8  $\mu$ L of plasmid encoding for mouse VEGFR2 (Meissirel et al., 2011) and 9  $\mu$ L of Plus reagent, incubated for 5min, and supplemented with 232  $\mu$ L OptiMEM and 18  $\mu$ L of LTX (Lipofectamine). This transfection preparation was then added to the cells in each Petri dishes and incubated for 24h at 37°C and 5% CO<sub>2</sub>. VEGFR2 expressing HEK cells obtained by transfection were deprived in SVF 12h before A $\beta$  and/or VEGF treatments to limit VEGF supply present in SVF. Cells were treated for 5 min with A $\beta$ m (1  $\mu$ M), used as a control or A $\beta$ o (1  $\mu$ M), with or without VEGF<sub>165</sub> (50 ng.mL<sup>-1</sup>). After treatments, HEK cells were washed and incubated in 600  $\mu$ L of lysis buffer (Tris HCL 25mM, EDTA 5mM, DOC 0.5mM, NP 40 1%, SDS 0.1%, NaCl 150mM), supplemented with cOmplete protease inhibitor cocktail 2%, Benzonase 0.02%, Orthovanadate 2%, and phosphatase inhibitors 2% for 10 min at 4°C. Cell lysates were then centrifuged at 10,000 g for 10min at 4°C to remove cellular debris, and stored at –20°C until use.

### Hippocampal neuron treatment

For biochemical assessment of receptor activation, post-synaptic enrichments and immunocytochemistry, hippocampal neuron cultures were used after 14–15 days *in vitro* (DIV) and treated for 1h with 1  $\mu$ M synthetic A $\beta$ <sub>142</sub> oligomers (A $\beta$ o) or their control peptides, with or without 50 ng/mL of VEGF<sub>165</sub>. A $\beta$  synaptic targeting was assessed by immunocytochemistry and cultures were treated for only 30 minutes with 500 nM synthetic A $\beta$ o or A $\beta$  monomers (A $\beta$ m), supplemented or not with 50 ng/mL of VEGF<sub>165</sub>. In some experiments designed to study GluA1 expressing receptor activation, neuron cultures were used after 21 DIV and treated for 12h with A $\beta$ o  $\pm$  VEGF<sub>165</sub>. Finally, for morphological analysis, cultures were treated at 17–18 DIV with 500 nM A $\beta$ o or their control peptides, with or without 50 ng/mL VEGF<sub>165</sub>, for 24 h.

## POSTSYNAPTIC DENSITY ENRICHMENT AND IMMUNOBLOTTING

### PSD enrichment

Postsynaptic density (PSD) fractions were prepared from control and treated 14–15 DIV hippocampal cell cultures, 1 hour after treatments, or from hippocampal samples from 4 and 8-month-old *APP/PS1* and WT mice. Hippocampal neurons were rinsed twice with cold D-PBS, harvested in cold buffer containing 0.32 M sucrose and 10 mM HEPES, cOmplete protease inhibitor cocktail, 2mM Sodium orthovanadate, complemented with a phosphatase inhibitor cocktail at pH 7.4, and centrifuged twice at 800 g for 10 min to remove nuclei and large debris. A supernatant fraction of 10  $\mu$ L per sample was collected for total lysate immunoblotting. Crude membrane fractions were obtained after a 12,000 g centrifugation step for 20 min, resulting pellets were resuspended in EDTA buffer to chelate calcium (4 mM HEPES, 1 mM EDTA, pH 7.4) and subsequently centrifuged twice at 12,000 g for 20 min to pellet synaptosomal fraction. Pellets were then incubated in a low-triton buffer for 1 hour (20 mM HEPES, 100 mM NaCl, 0.5% Triton X-100, pH 7.2) and centrifuged at 12,000 g. The supernatants contained the non-postsynaptic density fraction (non-PSD). The resulting pellets were further extracted with a high-detergent buffer during 1 hour (20 mM HEPES, 0.15 mM NaCl, 1% Triton X-100, 1% deoxycholic acid, 1% SDS, pH 7.5) and centrifuged 15 minutes at 10,000 g to obtain the postsynaptic density fraction (PSD) in the supernatants. Total lysate samples were lysed in 50 mM Tris-HCL, 150 mM NaCl, 1 mM EDTA, 1% NP-40, 0.5% deoxycholate, 0.1% SDS, pH 7.5 and all samples were kept at –20°C until use.

### Immunoblotting

PSD and non-PSD fractions (5–10  $\mu$ g of proteins) were subjected to immunoblotting analysis using 3%–8% or 4%–12% gradient SDS-PAGE gels for glutamate receptor or signaling protein analysis, respectively. Total lysates (7.5–10  $\mu$ g of proteins) were also separated on 4%–12% SDS-PAGE gels. Gels were transferred on nitrocellulose membranes and immunoblotted with dedicated

antibodies after a 45 minutes blocking step in Tris-buffered saline, 0.1% Tween, 5% milk or BSA, pH 7.6. Membranes were incubated overnight at 4°C with antibodies diluted in Tris-buffered saline, 0.1% Tween, pH 7.6, with 2% milk or 2% BSA for total or phosphorylated protein detection, respectively. Appropriate horseradish peroxidase (HRP)-conjugated secondary antibodies were applied for 2h at room temperature. Proteins were visualized with an ECL detection system and band intensities quantified using a densitometric analysis with ImageJ software.

## IMMUNOHISTOCHEMISTRY AND HIPPOCAMPAL NEURON IMMUNOSTAINING

### Immunohistochemistry

Heterozygous *APP/PS1-21* and wild-type male mice were killed by decapitation after deep isoflurane gas anesthesia and brains were rapidly dissected and fresh frozen. Postmortem human brain samples through F2 prefrontal cortex were obtained from histologically confirmed AD cases and age-matched controls (Table S1). Frozen serial sections were cut with a Cryostat at 10 and 7 μm thick for mouse and human brains respectively, and were further processed for immunostaining. Briefly, sections were fixed in 4% PFA with 4% sucrose for 10 minutes and rinsed twice in PBS. In addition, three in 50<sup>th</sup> serial mouse brain sections were stained with 0.05% Thioflavin-S in 50% ethanol for 8 min to label dense-core plaques, washed twice in 80% ethanol for 5 min, and rinsed 3 times in PBS. Subsequently, sections were permeabilized in 0.3% Triton X-100 in PBS with 1% BSA and stained overnight at 4°C with antibodies directed against VEGF, β-amyloid, OC fibrillar Aβ oligomers, GFAP or CD68 expressing activated microglia. Next, they were incubated for 2 hours at room temperature with appropriate fluorescently conjugated secondary antibodies: Alexa Fluor 488 for Aβ, Alexa Fluor 555 for VEGF and Alexa Fluor 647 for GFAP or CD68 detection. For VEGF and OC double-immunostaining on human brain sections, sequential immunoreactions were carried out to be able to use primary antibodies raised in the same host species. After overnight incubation with the VEGF antibody, sections were incubated the next day for 2 hours in a saturating concentration of Alexa 555 goat anti-rabbit secondary antibody to bind all sites of the VEGF antibody. OC immunostaining was completed on the third day. Controls were performed without any or with each of the primary antibodies. Before DAPI counterstaining, human sections were processed for an additional autofluorescence quenching step in 0.1% Sudan Black B in 70% ethanol for 10 minutes to decrease lipofuscin fluorescence. Finally, sections were counterstained with DAPI prior to mounting them with FluorSave reagent.

### Hippocampal neuron immunostaining

Hippocampal neuron cultures were grown on poly-L-lysine-coated glass coverslips for 14-15 DIV to analyze surface receptor expression, or 17-18 DIV for morphological analysis. Culture were fixed with 4% paraformaldehyde, 4% sucrose in 0.1 M phosphate buffer at RT prior to immunostaining under non-permeabilizing (cell surface GluA1 immunostaining) or permeabilizing (GFP immunostaining) conditions. After a blocking step in non-permeabilizing (PBS, 1% BSA) or permeabilizing (PBS, 0.3% Triton X-100, 1% BSA) buffer, antibodies recognizing the extracellular domain of GluA1 or GFP were used overnight at 4°C in appropriate blocking solution. After rinses, cells were incubated with appropriate Alexa conjugated secondary antibody combined or not with Alexa fluor 546 phalloidin for 2 hours at RT. Cultures were subsequently counterstained with DAPI and mounted in FluorSave reagent.

### Hippocampal neuron transfection for 3D confocal imaging

11 DIV hippocampal neurons were transfected with a pEGFP-C1 plasmid coding for enhanced green fluorescent protein (eGFP) under a CMV promoter (GenBank Accession #: U55763), using Lipofectamine LTX. Briefly, cells were treated with a mix including LTX, DNA and Plus reagent in OptiMEM. Transfection medium was removed after 5h and replaced with fresh Neurobasal medium supplemented with L-glutamine (2 mM), 2% B27, without antibiotics, for 24h. Next, half of the medium was changed for fresh supplemented Neurobasal medium with antibiotics. Hippocampal neurons were treated at 6 days post-transfection for 24h with Aβ or control peptide, supplemented or not with VEGF.

## IMAGE ACQUISITION AND ANALYSIS

### Imaging of brain section and cell surface immunostainings

Images were obtained using a Zeiss Imager Z1 equipped with Apotome technology for human brain section and hippocampal cell surface immunostainings, and with a slide scanner Axio Scan.Z1 for immunostaining of transgenic mice brain sections. For each image acquisition system identical acquisition parameters were used between treated conditions, and images were further analyzed with ImageJ software. To assess GluA1 surface expression, regions of interest (ROIs) were centered on the dendrite of hippocampal neurons in which F-actin cytoskeleton was labeled using Alexa fluor 555 phalloidin, and the density as well as the size of GluA1 clusters was quantified in each ROI in collapsed Z stacks. GluA1 surface clusters were defined as fluorescence signal being fivefold above background fluorescence and ranging from 0.25 to 0.60 μm in diameter. Data were expressed as density of GluA1 positive clusters per surface area or as size of GluA1 positive clusters, and by density of Thioflavin-S positive plaques, with or without VEGF expression.

### Confocal imaging of dendritic spines

For 3D dendritic spines analysis, hippocampal pyramidal cells expressing eGFP were selected based on their morphology and imaged using a confocal Leica TCS-SP5 X microscope equipped with a white light laser, a 63x objective and an additional zoom factor (3x). 3D confocal z stack images were analyzed using Imaris Software. Image acquisition and subsequent analyses were performed by an investigator blind to cell culture treatments.

### 3D dendritic spine modeling

Z stack images were subsequently deconvolved using Huygens software, and spine density and morphology were analyzed with Imaris software. Briefly, fragments of secondary and tertiary apical dendrites were selected and modeled with filament tracer with a total of 198 dendritic fragments measuring 27  $\mu\text{m}$  in average that have been analyzed for 66 hippocampal pyramidal cells. After automatic image thresholding, quantification and classification of spines were performed with Spine Classification MATLAB plugin. Five algorithms were used to classify spines according to Imaris measured parameters: Stubby spines:  $\text{length}(\text{spine}) < 0.7$  and  $2 * \text{min\_width}(\text{spine}) > \text{max\_width}(\text{head})$ ; Mushroom spines:  $\text{max\_width}(\text{head}) > \text{min\_width}(\text{spine}) * 2$  and  $\text{length}(\text{neck}) < \text{max\_width}(\text{head}) * 2$ ; Thin spines:  $\text{max\_width}(\text{head}) > \text{min\_width}(\text{spine}) * 1.5$  and  $\text{length}(\text{neck}) > \text{max\_width}(\text{head}) * 2$ ; Filopodia:  $1.3 * \text{mean\_width}(\text{neck}) > = \text{mean\_width}(\text{head})$  and  $\text{length}(\text{spine}) > 2$ ; Others: true. All spines which remained unclassified (around 10%), due to their ambiguous shape, were classified as “Others” and integrated to the total spine density analysis.

### Confocal imaging of synaptic targeting

For analysis of A $\beta$  synaptic targeting, images were obtained using a TCS-SP5X confocal microscope equipped with a 63x objective and an additional zoom factor (3x) under identical acquisition parameters. Images were subsequently deconvolved using Huygens Professional software and analyzed with Icy software. Image thresholding was applied for each channel to remove noise and Spot Detector plugin was used to detect significant signal. Detected spots or clusters were defined as region of interest (ROI) and subsequently launched with Colocalization studio plugin to assess the percentage of colocalized clusters. Data were expressed as density of PSD95, Bassoon or A $\beta$  positive clusters per 100  $\mu\text{m}^2$  surface area and by percentage of colocalized clusters.

## QUANTIFICATION AND STATISTICAL ANALYSIS

All data were expressed as mean  $\pm$  SEM, unless stated otherwise. Normality and variance homogeneity were assessed with descriptive statistics and appropriate tests using R and OriginLab softwares. Sample size ( $n$ ) was determined based on previous studies from the literature and pilot experiments;  $n$  refers to wells per condition in biochemical experiments, coverslips per condition in dendritic spine and cluster cell surface analyses, and mice per condition or per genotype for electrophysiological experiments. For protein activation, PSD, cluster density and dendritic spine analyses, protein expression level as well as cluster and spine density were compared for statistical significance between groups using a one-way ANOVA followed by a Tukey's post hoc test or a Kruskal Wallis and a Dunn's post hoc test when the assumptions of ANOVA were not met (R software). For ELISA assay, significant differences between curves were assessed comparing fits of nonlinear regression models for saturation binding curves using a  $F$  test (Prism, GraphPad). For electrophysiological recordings, statistical analysis of differences in fEPSP slopes between treatments was performed using a Kruskal Wallis followed by a Dunn's post hoc test, and a two-tailed paired  $t$  test to compare treatment effects with baseline. Statistical measure such as the mean  $\pm$  SEM, sample size ( $n$ ) and significance levels  $p < 0.05$ ,  $p < 0.01$ ,  $p < 0.001$  are provided in [Table S3](#).

**Cell Reports, Volume 35**

**Supplemental information**

**VEGF counteracts amyloid- $\beta$ -induced  
synaptic dysfunction**

**Laurent Martin, Pauline Bouvet, Naura Chounlamountri, Chantal Watrin, Roger Besançon, Delphine Pinatel, David Meyronet, Jérôme Honnorat, Alain Buisson, Paul-Antoine Salin, and Claire Meissirel**

<b>Case ID</b>	<b>Age</b>	<b>Sexe</b>	<b>Postmortem Delay</b>	<b>Neuropathological diagnosis</b>
Control 1	36	M	6 h 5 min	Lesions of the third ventricle
Control 2	52	F	33 h 5 min	Lesions of the third ventricle
Control 3	58	F	18 h 15 min	Cerebellar lesions
Control 4	50	F	26 h 30 min	Cerebellar lesions
AD 5	48	F	15 h 15 min	AD (Thal 5 – Braak V-VI)
AD 6	71	F	24 h 50 min	AD (Thal 5 – Braak V-VI)
AD 7	82	F	10 h 50 min	AD (Thal 5 – Braak V-VI)
AD 8	72	F	56 h	AD (Thal 5 – Braak V-VI)

**Table S1. Related to Figure 1**

Immunostainings	<b>Figure</b>	<b>1 A</b>	<b>1C, S1A</b>	<b>S4 B</b>	<b>7 B, D</b>	<b>8 C</b>	<b>S3 B</b>	
	Independent experiments	4	2	2	3	3	2	
	Human brain samples	4						
	Mouse brain sample per group		3					
	Cell culture seeding density			18.75 10 <sup>3</sup> cells/cm <sup>2</sup>	50 10 <sup>3</sup> cells/cm <sup>2</sup>	50 10 <sup>3</sup> cells/cm <sup>2</sup>	18.75 10 <sup>3</sup> cells/cm <sup>2</sup>	
	Wells per condition				Ctrl : 8 A $\beta$ o : 9 Ctrl+V : 7 A $\beta$ o+V : 7		A $\beta$ m : 6 A $\beta$ o : 6 A $\beta$ m+V : 5 A $\beta$ o+V : 4	
	Coverslips per condition			Ctrl : 7 A $\beta$ o : 9 Ctrl+V : 8 A $\beta$ o+V : 10	Ctrl : 8 A $\beta$ o : 9 Ctrl+V : 7 A $\beta$ o+V : 7			
Biochemistry	<b>Figure panels</b>	<b>2 A</b>	<b>2 B, D</b>	<b>3 B</b>	<b>3 B, D</b>	<b>4 B</b>	<b>4 D</b>	<b>4 F</b>
	Independent experiments	3	2 - 4	7	7	GluA1 : 10 GluN2A : 9	CaMKII : 5 Fyn : 8 Cal A : 7 Casp 3 : 4	GluA1 S845 : 10 GluA1 S831 : 9
	Cell culture density			50 10 <sup>3</sup> cells/cm <sup>2</sup>	50-70 10 <sup>3</sup> cells/cm <sup>2</sup>	70 10 <sup>3</sup> cells/cm <sup>2</sup>	70 10 <sup>3</sup> cells/cm <sup>2</sup>	70 10 <sup>3</sup> cells/cm <sup>2</sup>
	Slide per condition		4					
	Wells / dishes per condition	9		7	7-14	GluA1 : 10 GluN2A : 9	CaMKII : 10 Fyn : 16 Cal A : 14 Casp 3 : 14	GluA1 S845 : 10 GluA1 S831 : 9
Electrophysiology	<b>Figure panels</b>			<b>5 A, B</b>	<b>5 C, D</b>	<b>5 E, F</b>	<b>5 G, H</b>	<b>6 A – D</b>
	Independent experiments			Ctrl : 5 VEGF : 5 A $\beta$ o : 5 A $\beta$ o+V : 5	Ctrl : 5 VEGF : 5 A $\beta$ o : 7 A $\beta$ o+V : 7	WT : 7 VEGF : 7 APP/PS1 : 7 VEGF : 7	WT : 7 VEGF : 7 APP/PS1 : 6 VEGF : 6	Ctrl : 8 - 5 VEGF : 6 - 5 A $\beta$ o : 10 - 5 A $\beta$ o+V : 9 - 6
	Mice per experiment per genotype			Ctrl : 5 VEGF : 5 A $\beta$ o : 5 A $\beta$ o+V : 5	Ctrl : 5 VEGF : 5 A $\beta$ o : 7 A $\beta$ o+V : 7	WT : 7 VEGF : 7 APP/PS1 : 7 VEGF : 7	WT : 7 VEGF : 7 APP/PS1 : 6 VEGF : 6	Ctrl : 8 - 5 VEGF : 6 - 5 A $\beta$ o : 10 - 5 A $\beta$ o+V : 9 - 6
	Hippocampal slices per condition per genotype			Ctrl : 9 VEGF : 7 A $\beta$ o : 8 A $\beta$ o+V : 6	Ctrl : 10 VEGF : 10 A $\beta$ o : 10 A $\beta$ o+V : 10	WT : 15 VEGF : 8 APP/PS1 : 15 VEGF : 10	WT : 14 VEGF : 14 APP/PS1 : 14 VEGF : 14	Ctrl : 8 - 5 VEGF : 7 - 5 A $\beta$ o : 12 - 5 A $\beta$ o+V : 10 - 6

**Table S2. Related to STAR Methods**

<b>Expression / phosphorylation of receptors and signaling proteins in HEK cells, neurons or PSDs</b>						
	<b>Aβm</b>	<b>Aβm+VEGF</b>	<b>Aβm vs Aβm+VEGF</b>	<b>Aβo</b>	<b>Aβo+VEGF</b>	<b>Aβo vs Aβo+VEGF</b>
VEGFR2 phosphorylation in HEK cells (%)	100.00 ± 20.62	275.90 ± 22.80	p<0.01 n=7-7	80.13 ± 9.08	161.70 ± 11.77	p<0.05 n=7-7
	<b>Ctrl</b>	<b>Aβo</b>	<b>Ctrl vs Aβo</b>	<b>Aβo</b>	<b>Aβo+VEGF</b>	<b>Aβo vs Aβo+VEGF</b>
VEGFR2 phosphorylation in neurons (%)	100.00 ± 6.85	36.99 ± 4.69	p<0.05 n=7-7	36.99 ± 4.69	98.66 ± 6.32	p<0.01 n=7-7
GluA1 expression in PSD (%)	100.00 ± 6.92	55.5 ± 9.17	p<0.01 n=10-10	55.50 ± 9.17	110.00 ± 12.60	p<0.01 n=10-10
Caspase-3 activation in PSD (%)	100.00 ± 6.35	205.60 ± 9.66	p<0.05 n=7-7	205.60 ± 9.66	76.70 ± 14.38	p<0.001 n=7-7
Calcineurin activation in PSD (%)	100.00 ± 9.83	191.60 ± 15.28	p<0.01 n=7-7	191.60 ± 15.28	112.60 ± 7.71	p<0.05 n=7-7
GluA1 S845 phosphorylation in 15 DIV neurons (%)	100.00 ± 4.85	65.90 ± 4.56	p<0.0001 n=10-10	65.90 ± 4.56	98.75 ± 3.74	p<0.0001 n=10-10
GluA1 S845 phosphorylation in 21 DIV neurons (%)	100.00 ± 6.02	66.17 ± 8.41	p<0.01 n=8-8	66.17 ± 8.41	91.91 ± 5.26	p<0.05 n=8-8
<b>Basal synaptic transmission</b>						
	<b>Control</b>	<b>VEGF</b>	<b>Ctrl vs VEGF</b>	<b>Aβo</b>	<b>Aβo+VEGF</b>	<b>Aβo vs Aβo+VEGF</b>
Slope of I/O curve	1.37 ± 0.21	1.31 ± 0.24	n.s. n=5-5	0.74 ± 0.20	1.12 ± 0.18	n.s. n=5-5

		<b>VEGF</b>	<b>VEGF vs Ctrl baseline</b>		<b>A<math>\beta</math>+VEGF</b>	<b>A<math>\beta</math>+VEGF vs A<math>\beta</math> baseline</b>
mean fEPSP (%) versus baseline		96.1 $\pm$ 10	<i>n.s.</i> <i>n</i> =5		126 $\pm$ 10	<i>p</i> <0.05 <i>n</i> =7
	<b>WT</b>	<b>WT+VEGF</b>	<b>WT vs WT+VEGF</b>	<b>APP/PS1</b>	<b>APP/PS1+VEGF</b>	<b>APP/PS1 vs APP/PS1+VEGF</b>
Slope of I/O curve	1.23 $\pm$ 0.18	1.21 $\pm$ 0.17	<i>n.s.</i> <i>n</i> =7	0.64 $\pm$ 0.11	1.19 $\pm$ 0.14	<i>p</i> <0.01 <i>n</i> =6
			<b>VEGF vs WT baseline</b>		<b>APP/PS1+VEGF</b>	<b>VEGF vs APP/PS1 baseline</b>
mean fEPSP (%) versus baseline		118.41 $\pm$ 6.4	<i>p</i> <0.05 <i>n</i> =7		136.16 $\pm$ 8.2	<i>p</i> <0.01 <i>n</i> =6
<b>LTP amplitude</b>						
	<b>Ctrl</b>	<b>A<math>\beta</math></b>	<b>Ctrl vs A<math>\beta</math></b>	<b>A<math>\beta</math></b>	<b>A<math>\beta</math>+VEGF</b>	<b>A<math>\beta</math> vs A<math>\beta</math>+VEGF</b>
mean fEPSP (%)	278.46 $\pm$ 26.38	146.85 $\pm$ 17.11	<i>p</i> <0.01 <i>n</i> =8-10	146.85 $\pm$ 17.11	307.11 $\pm$ 75.01	<i>p</i> <0.05 <i>n</i> =10-9
<b>LTD amplitude</b>						
		<b>A<math>\beta</math></b>	<b>A<math>\beta</math> vs A<math>\beta</math> baseline</b>		<b>A<math>\beta</math>+VEGF</b>	<b>A<math>\beta</math>+VEGF vs A<math>\beta</math>+VEGF baseline</b>
mean fEPSP (%) versus baseline		73.25 $\pm$ 8.53	<i>p</i> <0.05 <i>n</i> =5		104.9 $\pm$ 21.8	<i>n.s.</i> <i>n</i> =6

<b>Spine density</b>						
	<b>Ctrl</b>	<b>A<math>\beta</math>o</b>	<b>Ctrl vs A<math>\beta</math>o</b>	<b>A<math>\beta</math>o</b>	<b>A<math>\beta</math>o+VEGF</b>	<b>A<math>\beta</math>o vs A<math>\beta</math>o+VEGF</b>
Total spines per $\mu\text{m}$	1.71 $\pm$ 0.07	1.15 $\pm$ 0.07	p<0.001 n=8-9	1.15 $\pm$ 0.07	1.60 $\pm$ 0.08	p<0.01 n=9-7
Mushroom spines per $\mu\text{m}$	0.35 $\pm$ 0.03	0.12 $\pm$ 0.02	p<0.01 n=8-9	0.12 $\pm$ 0.02	0.35 $\pm$ 0.03	p<0.01 n=9-7

**Table S3. Related to Figure 3, 4, 5, 6 and 7**

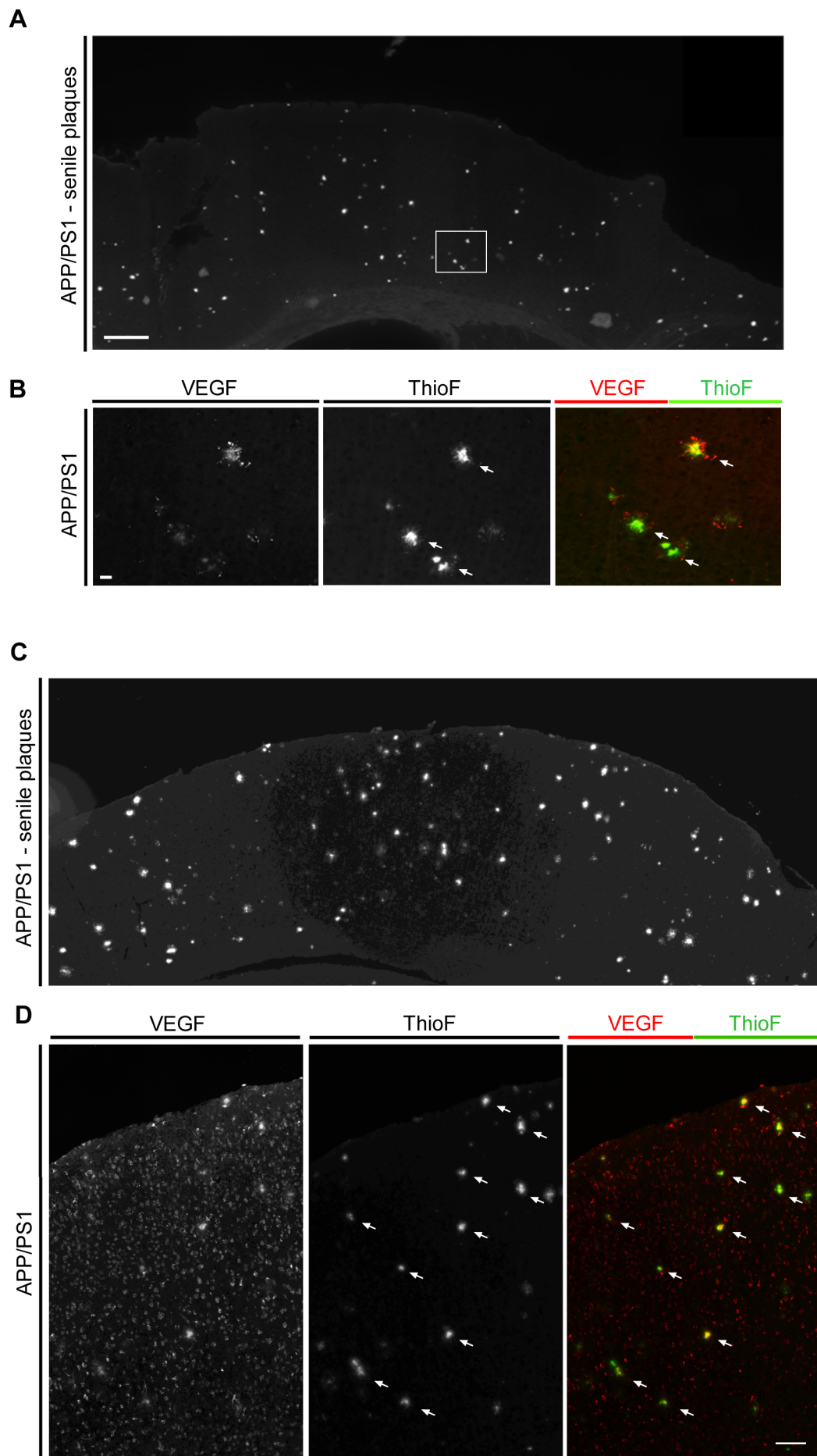


Figure S1. Related to Figure 1

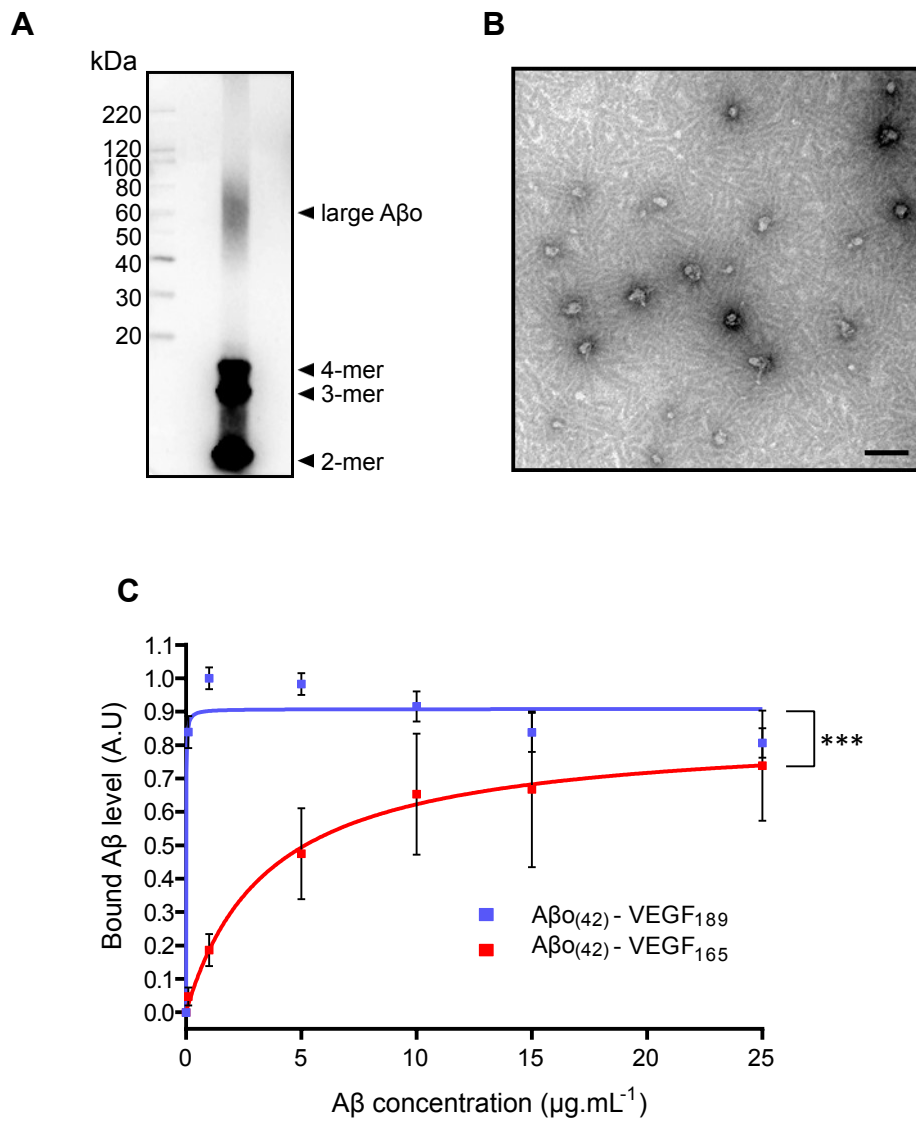
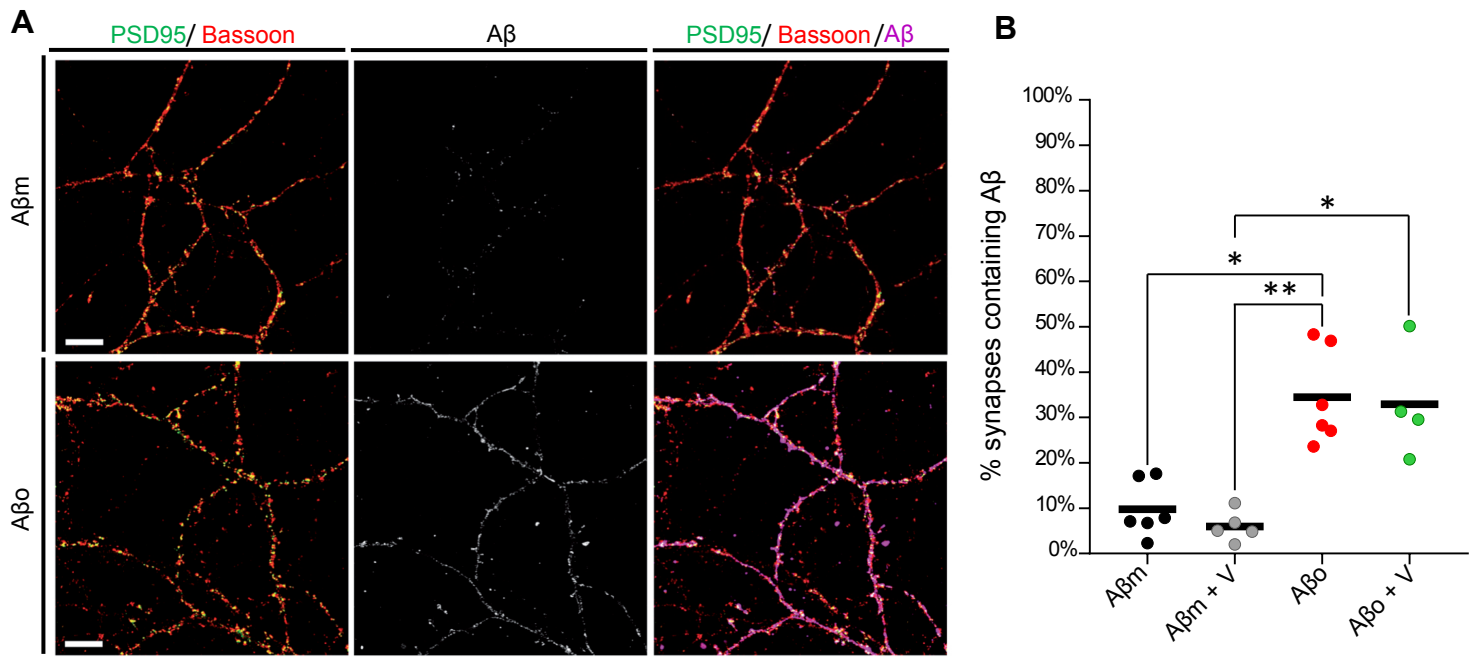


Figure S2. Related to Figure 2.



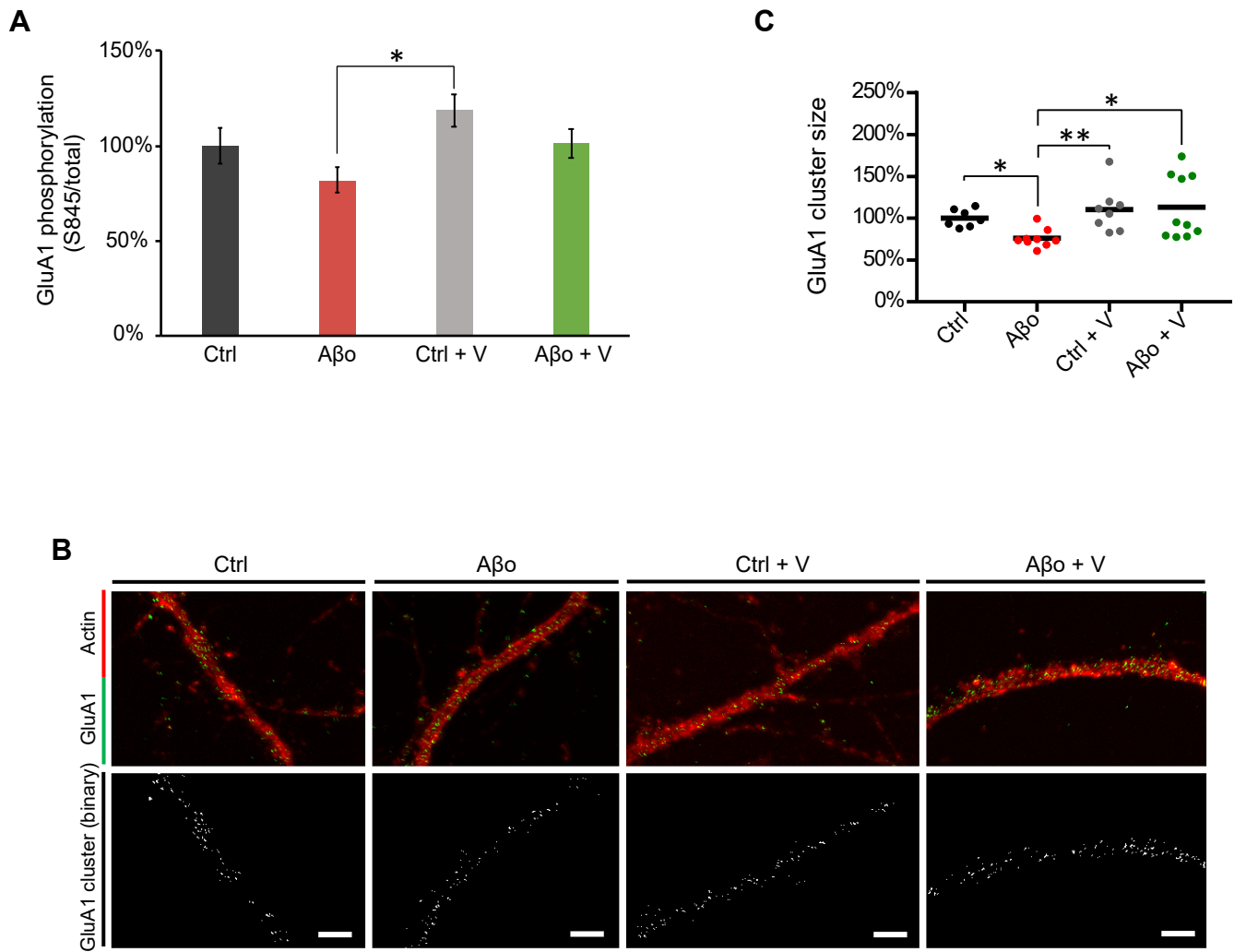


Figure S4. Related to Figure 4

**Table S1. Related to Figure 1.** Histopathological information on brain samples used for immunohistopathological analysis in Figure 1A.

**Table S2. Related to STAR Methods.** The sample size ( $n$ ) and the number of independent experiments used in the Figures of the paper are reported. In addition, the density of hippocampal cell cultures and the number of acute hippocampal slices used in the experiments are described.

**Table S3. Related to Figures 3, 4, 5, 6 and 7.** Normalized expression or phosphorylation status of receptors and signaling proteins derived from cultured HEK cells and hippocampal neurons in treated conditions. Data are presented as means  $\pm$  SEM and refer to Figure 3 and 4 for statistical comparisons. Basal synaptic transmission and long-term synaptic potentiation or depression amplitudes in treated hippocampal slices derived from WT or *APP/PS1* mice. Data are presented as slopes of I/O curves or normalized fEPSP slopes (means  $\pm$  SEM) and refer to Figure 5 and 6 for statistical comparisons. Total spine density and density of mushroom spines in treated conditions. Data are expressed as means  $\pm$  SEM and refer to Figure 7 for statistical comparisons.

**Figure S1. Related to Figure 1. Accumulation of VEGF in amyloid plaques increased with A $\beta$  burden in *APP/PS1* mice.** **A)** Brain A $\beta$  plaque burden in *APP/PS1* transgenic mice. Representative brain section from 4-month-old transgenic mice showing Thioflavin-S positive extracellular amyloid deposits in the cerebral cortex. **B)** Higher-magnification of individual plaques delineated in white (**A**) showing a Thioflavin-S positive plaque (middle) immunoreactive for VEGF (left) with the colocalization in the merge (right). White arrows point to A $\beta$ -positive plaques detected by Thioflavin-S. Scale bar, 50  $\mu$ m. **C)** Numerous Thioflavin-S positive plaques covering the entire neocortex in 8-month-old male *APP/PS1* transgenic mice. Note the aggravated plaque burden in 8-month-old mice compared to the one found at 4 months of age with larger dense-core amyloid deposits. **D)** High magnification of representative plaques taken from (**C**) showing VEGF expression (left) in Thioflavin-S positive plaques (middle), with the colocalization in the merge (right). Scale bar C, 180  $\mu$ m; D, 100  $\mu$ m.

**Figure S2. Related to Figure 2. Characterization of A $\beta$  preparations and their interactions with heparin-binding VEGF isoforms.** **A)** Oligomeric preparations of synthetic A $\beta$ <sub>42</sub> were subjected to SDS-PAGE electrophoresis and immunoblotted using the anti-A $\beta$  6E10

antibody. Representative immunoblotting showing dominant bands corresponding to monomeric (1-mer), trimeric (3-mer) and tetrameric (4-mer) A $\beta$  forms, together with smear bands from 30 to 80kDa reflecting large A $\beta$ . **B)** Representative transmission electron micrograph of negatively stained synthetic A $\beta$  sample exhibiting typical rounded structured oligomers. Scale bar, 100 nm. **C)** ELISA assay showing a dose-dependent binding of biotinylated forms of A $\beta$ <sub>42</sub> oligomers (A $\beta$ ) to the heparin-binding VEGF isoforms VEGF<sub>165</sub> and VEGF<sub>189</sub>. The HRP-TMB reaction-based colorimetric method was used to detect binding. Each value represents the mean  $\pm$  SEM between independent experiments,  $n=3-4$  for VEGF<sub>165</sub> and VEGF<sub>189</sub>, respectively; \*\*\* $<0.001$ .

**Figure S3. Related to Figure 3. VEGF does not influence A $\beta$  synaptic targeting.** **A)** Representative confocal images of immunostainings for PSD95 (green), Bassoon (red) and A $\beta$  (white or magenta) performed on DIV 12 hippocampal neurons treated with A $\beta$ m (used as a control, upper panels) or A $\beta$ o (lower panels). Co-localization of presynaptic Bassoon and postsynaptic PSD95 clusters delineating full synapses is shown on left, A $\beta$  cell surface staining in the middle and the merge on right. Note the selective A $\beta$ o binding to hippocampal neuron cell surface. **B)** Quantitative analysis of synapses containing A $\beta$  positive clusters in all conditions: A $\beta$ m ( $n=6$  coverslips), A $\beta$ m+VEGF ( $n=5$ ), A $\beta$ o ( $n=6$ ), A $\beta$ o+VEGF ( $n=4$ ). Statistical significance was assessed using Kruskal-Wallis and Dunn's *post-hoc* test, (Kruskal-Wallis  $p=0,0015$ , from 2 independent experiments. \* $< 0.05$ , \*\* $<0.01$ ).

**Figure S4. Related to Figure 4. A $\beta$ o-induced alterations in AMPA-R phosphorylation and surface expression, with opposite effects of VEGF.** **A)** GluA1 phosphorylation status in acute adult hippocampal slices after pretreatment with or without 500 nM A $\beta$ o $\pm$ VEGF for 40 minutes and induction of chemical LTP (cLTP) by 25 mM TEA for 10 minutes. Semi-quantitative analyses obtained by Western Blotting showing the level of GluA1 S845 phosphorylation in total hippocampal lysates derived from treated slices 60 minutes after cLTP. All values were normalized to control and expressed as mean  $\pm$  SEM. Statistical significance was assessed using a one-way ANOVA with a *post-hoc* Tukey's test (one-way ANOVA  $p=0.015$ ,  $n=15$  independent experiments). \* $< 0.05$ . **B), C)** Hippocampal neuronal cultures treated for 1 hour with control peptides (Ctrl) or A $\beta$  oligomers (A $\beta$ ) at 1  $\mu$ M, with or without 50 ng.mL<sup>-1</sup> VEGF, were processed for surface GluA1 immunostaining and F-actin labeling. **B)** Upper panels illustrating a representative dendritic staining for GluA1 (green) and F-actin (red) in all

conditions. Binary images in the lower panels are depicting labelled GluA1 surface clusters with a fluorescence signal fivefold above background fluorescence and a size ranging from 0.25 to 0.60  $\mu\text{m}$  in diameter. Scale bar, 2.5  $\mu\text{m}$ . C) Quantitative analysis indicates mean values of GluA1 cluster size with data normalized to control and analyzed for statistical significance using a Kruskal-Wallis and Dunn's *post-hoc* test (Kruskal-Wallis  $p=0.0035$ ,  $n=7-10$ ).  $\text{A}\beta_0$  induced a reduction in GluA1 cluster size ( $75.99\pm 3.64\%$  with  $\text{A}\beta_0$  vs  $100.00\pm 3.98\%$  in Ctrl, *post-hoc*  $p<0.05$ ,  $n=9-7$ ) counteracted by VEGF ( $113.10\pm 12.02\%$  with  $\text{A}\beta_0+\text{VEGF}$  vs  $75.99\pm 3.64\%$  with  $\text{A}\beta_0$ , *post-hoc*  $p<0.05$ ,  $n=10-9$ ). \* $< 0.05$ , \*\* $<0.01$ .